

Astronomically tuned magnetocyclostratigraphy of late Burdigalian marine sediments at Monte Cardeto, Ancona, Italy

By:
T. E. Van Peer

Supervisor:
Dr. S.K. Hüsing

Co-supervisors:
Dr. F.J. Hilgen
Prof. Dr. W. Krijgsman

July 2013
Utrecht University

1. Abstract

The hemipelagic Monte Cardeto – Spiaggia della Scalaccia composite section is characterised by cyclic marl-limestone alternations, astronomically tuned between 17.08 and 16.18 Ma (late Burdigalian). The natural remanent magnetization is carried by greigite, based on IRM acquisition curves, thermomagnetic runs and thermal demagnetization. The resulting magnetostratigraphy reveals a straightforward correlation to subchrons C5Cr to C5Cn.1n of the Geological Time Scale 2012 (GTS2012). Spectral and wavelet analyses are performed to validate the cyclicity in the depth domain, which is transferred into the time domain using a first order age model with the ages of reversals from GTS2012. Wavelet and spectral analysis in the time domain confirm astronomically driven marl-limestone alternations.

Based on CaCO_3 content, Rb/Sr, Ba/Al, Ti/Al, Zr/Al, Mn/Al, V/Al, Si/Al and specific magnetic susceptibility, the limestones are correlated to insolation maxima (boreal precession minima). The reversal ages, originally used in the first order age model, are revised by tuning the Ca/Al and Rb/Sr records to the La2001_(1,0.9) solution by first recognizing the eccentricity cycles, followed by the precession and obliquity cycles. This results in astronomically derived ages of the reversals between C5Cr and C5Cn.1n, which should replace the GTS2012 reversal ages. Furthermore, this high resolution age model enables the recognition of carbon isotope events CM1-CM3a and the oxygen isotope shift at the onset the Middle Miocene Climatic Optimum.

2. Introduction

The Miocene epoch is an important interval in Earth's climate history, characterized by the Mid-Miocene Climatic Optimum (MMCO) between *ca.* 17 and 15 Ma, followed by the Middle Miocene Climatic Transition (MMCT, characterized by cooling) up to *ca.* 10 Ma [Zachos *et al.*, 2001]. These Middle Miocene climate events coincide with a large positive $\delta^{13}\text{C}$ excursion, called the "Monterey Excursion" between *ca.* 16.9 and 13.5 Ma [Abels *et al.*, 2005; Holbourn *et al.*, 2007], reflecting global organic carbon burial in regions with upwelling and therefore enhanced primary productivity [Diester-Haass *et al.*, 2009 and references therein]. Superimposed on the Monterey Excursion, smaller scale $\delta^{13}\text{C}$ excursions occur, labelled CM1-CM6 [Woodruff and Savin, 1991], consisting of nine successive *ca.* 405 kyr eccentricity cycles [Holbourn *et al.*, 2007]. The Miocene is also characterized by prominent, positive oxygen-isotope events, called Mi1-Mi6, marking several short, but significant climate changes [Miller *et al.*, 1991; Miller and Mountain, 1996]. Additional positive oxygen isotope excursions are identified and labelled with an additional letter, such as Mi1b and Mi1c [Scott *et al.*, 1995].

Since these isotopes excursions represent (palaeo)climatic changes, high-resolution age control is required to accurately determine the age and pace of the events and global causal relations. Unfortunately, many Early to Middle Miocene deep-sea records contain hiatuses [Keller and Barron, 1983; Woodruff and Savin, 1991], which makes a high-resolution age record very difficult. The marine hemipelagic sediments exposed at the Conero Riviera (just south of Ancona, Italy) provide an excellent record of the late Early to Late Miocene and the Middle to Late Miocene part of these sediments is already used for an improved geological timescale. Furthermore, these sediments have been used for dating of Middle Miocene oxygen events [Mourik *et al.*, 2010].

The end of the MMCO has been sampled from the base of C5Cn.1n (16.268 - 15.974 Ma) [Turco *et al.*, 2011; Hilgen *et al.*, 2012], but the onset of the MMCO, an important step in Miocene climate evolution, has not yet been sampled along these cliffs. In this paper the sedimentary record will be expanded further into the Burdigalian, covering the onset of the MMCO. A high-resolution age model, combining magnetostratigraphy, cyclostratigraphy and astronomical tuning, enables us to independently support and improve the currently published Geomagnetic Polarity Time Scale (GPTS) of Early Miocene reversal boundaries, which is used in dating sediments all over the world. The reversals of the magnetic field can be dated accurately using the changes in Earth's orbit (eccentricity) around the sun and the variations of Earth's axis (obliquity, precession) in a so-called astronomical tuning. This resulted in astronomically tuned ages down to *ca.* 15.2 Ma [Hüsing *et al.*, 2010] in the so-called GTS2012 [Hilgen *et al.*, 2012].

Astronomically tuned ages for Early Miocene magnetic reversals are not yet available. These ages are calculated based on an interpolation on spreading ridges [Lourens *et al.*, 2004]. In this paper an astronomical tuning of the late Burdigalian (*ca.* 17-16 Ma) is presented, covering the onset of the MMCO and subchrons C5Cr to C5Cn.1n. The precession cycle (required for the tuning) is defined by changes in several chemical ratios, magnetic susceptibility and the colour of the sediments, which are all related to variations in the insolation index. These variations in insolation have been modelled back in time [Laskar, 2001; Laskar *et al.*, 2004, 2011] and can thus be used for dating by matching sedimentary and proxy patterns with patterns observed in the insolation target curve.

3. Geological setting and section

3.1 Geological setting

The city of Ancona (Italy) (see Figure 1a) is located at a latitude of $43^{\circ}37'01''\text{N}$ and a longitude of $13^{\circ}31'00''\text{E}$ of Greenwich (WGS84) in the central part of Mediterranean basin, which was part of the western Tethys domain during the Early Miocene. Reconstructions of the palaeo-Mediterranean [Schettino and Turco, 2010] of the Miocene epoch show that this region was strongly influenced by the closure of the eastern (during the early Miocene) and western (during Messinian times) gateway [Rögl, 1998], caused by the convergence of the Eurasian and African plates.

Miocene sediments in this region are characterized by sedimentation of carbonates to marly carbonates with several volcanogenic beds [Kocsis et al., 2008; Guerrera et al., 2012], likely caused by the counter clockwise rotation of Sardinia [Assorgia et al., 1994; Beccaluva et al., 2004]. Around the same time, the continuity of the Miocene strata [Guerrera et al., 2012] was disturbed by a eastward directed progressive deformation front, forming the present-day Apennines. The front reaches the Marche region (which includes Ancona) in Pliocene times [Montanari et al., 1997b], so the Early to Late Miocene sediments are continuous (except a small hiatus at ca. 7.1 Ma [Hüsing et al., 2009b]). Near Ancona the exposure starts with the Early Miocene Burdigalian Bisciardo Formation [Montanari et al., 1997b], containing mainly calcareous deposits with some interbedded volcanoclastics.



Figure 1a (Upper): The locations of the Monte Cardeto subsection (locality A, north of Ancona) and the Spiaggia della Scalaccia subsection (locality B, southeast of Ancona). Figure is constructed using Google Earth.

Figure 1b (Lower): Aerial photograph of the Monte Cardeto subsection. Indicated are the different intervals and the top and base of the MCSS composite section.

On top of the Bisciaro Formation the Schlier Formation is exposed, with the boundary defined at a prominent, regionally present ash bed, called “Livello Piera della Francesca” [Coccioni and Montanari, 1992]. The Schlier formation is characterized by marly limestones, deposited at an estimated depth of *ca.* 600 m [Mader *et al.*, 2001]. Seven prominent beds (“Megabeds”), combined *ca.* 35 m thick, are present in the lower part of the Schlier Formation [Montanari *et al.*, 1997b], deposited during the latest Burdigalian to earliest Langhian [Turco *et al.*, 2011]. The intervals above and below the Megabeds are less prominent and characterized by cyclic marl-limestone alternations [Montanari *et al.*, 1997b]. The interval above the Megabeds has been used to improve the geological timescale [Hüsing *et al.*, 2007, 2010; Mourik *et al.*, 2010] and the Megabeds are still subject to research [S.K. Hüsing, F.J. Hilgen and E. Turco, *pers. comm.*].

3.2 Section

The Megabeds enable excellent correlations along the different bays along the cliffs south of Ancona (see Figure 1b). These seven beds are present at the base of the La Vedova section [Montanari *et al.*, 1997b] and the lowest two form the top of the so-called Monte Cardeto (MC) subsection (locality A in Figure 1a), which is subject to research in this paper. The Monte Cardeto subsection is exposed near the harbour of Ancona and roughly 50 m is well-exposed and sampled along the beach.

The downward continuation of the marine succession is exposed several kilometers southeast of Ancona, at the Scalaccia beach and will be referred to as the Spiaggia della Scalaccia (SdS) subsection (locality B in Figure 1a). At this location 25 m of sediment have been sampled, from a total of roughly 70 m accessible exposure [Kuikman, E. and Hüsing, S.K., *pers. comm.*]. A composite section, called MCSS (Monte Cardeto and Spiaggia della Scalaccia composite section), is constructed using the patterns in an interval of *ca.* 17 m (see Figure 2). The pattern can be best described by dividing the overlap in four short intervals, where 1) is the top of the overlap and 4) is the base: 1) a relatively thin (*ca.* 1 m) marl-limestone alternation at *ca.* 40-43 m; 2) a light grey marl at *ca.* 39 m; 3) thicker (*ca.* 1.5 m) marl-limestone alternations; 4) thick marl-limestone alternations (*ca.* 2-2.5 m).

Furthermore, the prominence of the limestones is variable (but decreasing) throughout the overlap. These limestones are indicated with an asterisk and their prominence as observed in the field (f=faint; n=normal; d=distinct; p=prominent). The top of SdS has been measured in a gully and therefore the thicknesses do not match exactly with those measured at MC. However, the position of the greyish marl relative to the change in thickness of the basic marl-limestone alternation and the change in prominence of the limestones provide evidence that the correlation is done correctly.

The MCSS composite section can be subdivided into three intervals based on lithological differences (see Figure 2). The lowermost part interval 1 (0-22 m) is characterized by an alternation of marls and marly limestones. Two more indurated sub-intervals are visible at *ca.* 5 to 9 m and at *ca.* 12 to 17 m, informally labelled “D” and “E” [E. Kuikman and S.K. Hüsing, *pers. comm.*]¹. In the upper positioned indurated “E”, at *ca.* 15 m, two very characteristic dark marls (at *ca.* 15.3 and 16.2 m) and a third, fainter marl (at *ca.* 14.5 m) are visible below the two prominent marls. The lower positioned indurated (but less than “E”) interval “D” is characterised by an upwards increase in prominence, with one very prominent, marly limestone bed at *ca.* 8 m. On top of “D” there is a marl exposed between *ca.* 9.5 and 12.5 m, which is relatively soft at base and top and more prominent in the middle.

The recognition of intricate sedimentary details in the Spiaggia della Scalaccia subsection was hampered by the fact that the entire subsection has been sampled in a gully, that was dug out of a landslide, partly covered by vegetation. Therefore details of a photographic log (using photographs when revisiting SdS in 2013) are included, which shows some additional details in particular in the lowest *ca.* 8 m.

¹ In total five prominent intervals (total thickness *ca.* 50 m to the top of interval 1) are recognised E. Kuikman and S.K. Hüsing [*pers. comm.*], informally labelled “A” to “E”. “A” is the stratigraphically lowest prominent interval exposed in this bay and only “D” and “E” are included in this research.

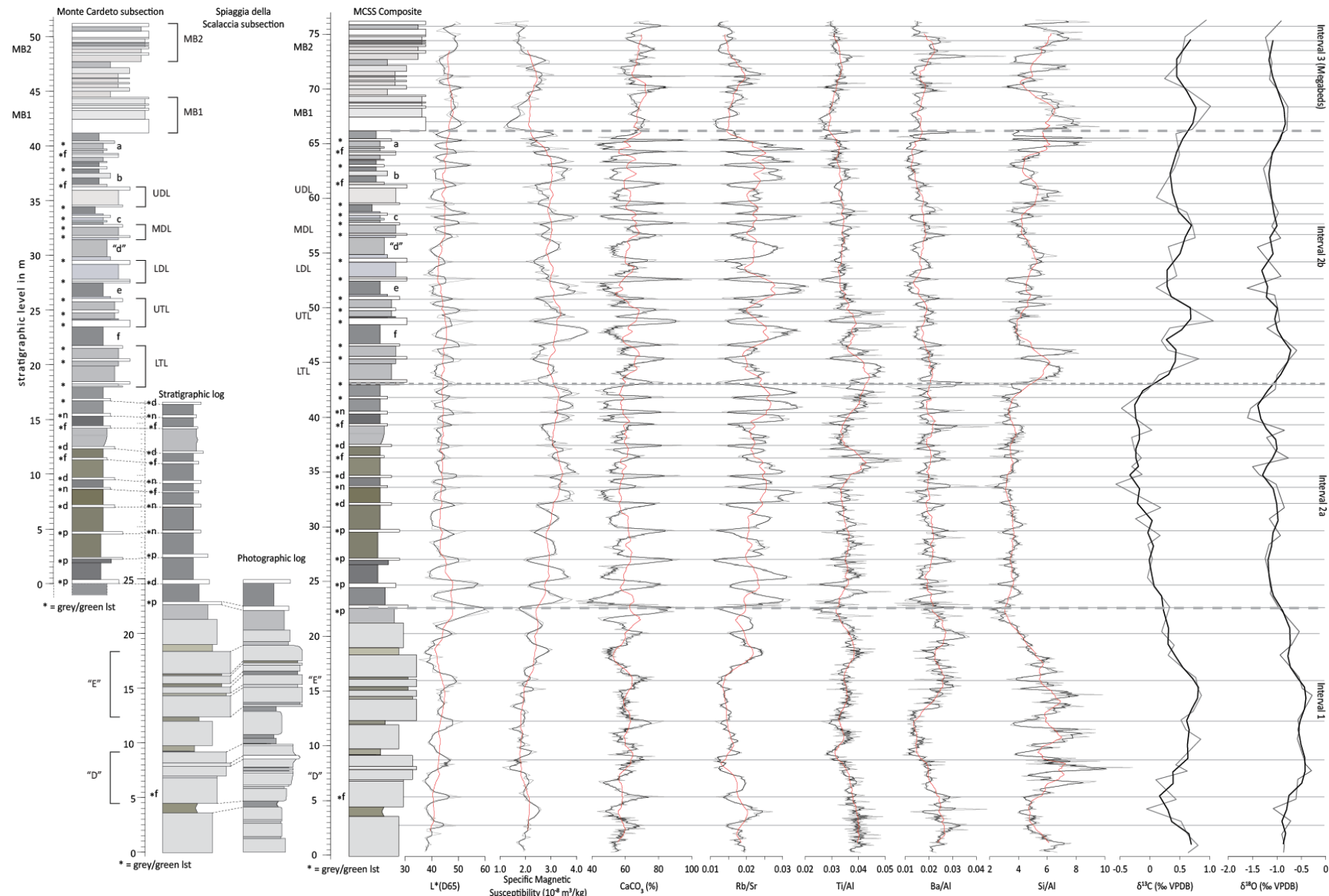


Figure 2: Stratigraphic log (in meters) of the Monte Cardeto and Spiaggia della Scalaccia subsections, with an additional photographic log of the sampled interval of the Spiaggia della Scalaccia subsection. Asterisks next to the log indicate the presence of a relatively coarse grained, greenish-greyish limestone and if available, its corresponding prominence (f=faint; n=normal; d=distinct; p=prominent). Horizontal lines are drawn through the maxima in CaCO_3 content, most of the times at the same position as a greenish-greyish limestone. The six darker marls ("a" to "f"), the grouped limestones (LTL=Lower Triple Limestone; UTL=Upper Triple Limestone; LDL=Lower Double Limestone; MDL=Middle Double Limestone; UDL=Upper Double Limestone) and the more prominent "D", "E" and Megabeds ("MB" I and II) are indicated next to the log. On top of the L*(D65), specific magnetic susceptibility, CaCO_3 content, Rb/Sr , Ti/Al , Ba/Al and Si/Al (grey) records a 3-point (black and 25-point (red) moving average are plotted. For $\delta^{13}\text{C}$ and $\delta^{18}\text{O}$ only the 3-point moving average is plotted. Note the division in intervals, as indicated on the right of the figure.

The transition from interval 1 to interval 2 is defined by a gradual change in prominence from the top of "E" to the lowest prominent limestone at *ca.* 22.5 m. At the same time the pattern changes from generally prominent marl(y limestone)s to clear marl and limestone alternations at the base of interval 2 and therefore the boundary between interval 1 and 2 is set at the last prominent marl below the first prominent limestone.

Interval 2 can be divided into two subintervals, of which the lower part of interval 2a (*ca.* 22.5-43 m) is characterised by a very prominent alternation of soft, dark, brown marls and distinct limestones. When these limestones are wet, the whitish weathering colour turns greenish-greyish. These limestones are marked in the log (see Figure 1) by an asterisk and their prominence, as observed in the field (f=faint; n=normal; d=distinct; p=prominent). In interval 2a the prominence of the limestones decreases from "prominent" at the lower half to "normal" at *ca.* 40 m. The colour of the marls becomes lighter up section from dark brownish to dark greyish, with the exception one more indurated, light greyish marl at *ca.* 39 m.

The *ca.* 2 m marl-limestone alternation decreases in thickness to *ca.* 1 m at 39 m (around the greyish marl). Just below the greyish marl the thickness pattern is not a constant decrease, there are two bundles (*ca.* 32-34.5 m and *ca.* 34.5-37.5 m) of *ca.* 2.5 m thickness. These bundles consist of *ca.* 1 m marl, with a (relative) less prominent limestone on top, followed by *ca.* 1.5-2 m marl and a (relative) more prominent limestone.

In interval 2b (43-66 m) green-greyish limestones continue to be present, but the marl-limestone alternation is replaced by an alternation of more indurated greyish marly limestones of *ca.* 2-4 m thickness and dark, brown marls. When wet, six prominent dark brown marls are clearly visible (labelled "a" to "f", where "d" is rather greyish). The lower two intervals with greyish marly limestones contain three green-greyish limestone beds and are informally labelled Lower Triple Limestone (LTL; *ca.* 43-47 m) and Upper Triple Limestone (UTL; *ca.* 49-51 m). The other more prominent marly limestone intervals only contain two green-greyish limestone beds and are thus informally labelled Lower Double Limestone (LDL; *ca.* 52.5-54.5 m), Middle Double Limestone (MDL; *ca.* 56.5-57.5 m) and Upper Double Limestone (UDL; *ca.* 59.5-61.5 m).

In the upper part of interval 2b a *ca.* 1 m marl-(whitish) limestone-marl-(green-greyish) limestone alternation is present. This alternation is present in darker marl "c" for the first time and continues into "b" and "a" as well as the interval between "b" and "a". In these intervals, the green-greyish limestones are more prominent than the whitish limestones, except the limestone in marl "b".

Interval 3 consists of the earlier mentioned Megabeds I and II, both roughly 3 m thick. These very prominent whitish marly limestones are characterized by a prominent base and thin, prominent beds inside a Megabed. Intercalated between these two Megabeds are thin beds of marls and (marly) limestone, with the thickness of one marl-limestone alternation being *ca.* 0.5 m. Two of those marls are softer and slightly thicker; a light grey marl is present just above Megabed I (at *ca.* 70 m) and darker grey marl below Megabed II (*ca.* 72.5 m).

4. Methods

A total of 405 (primary) oriented samples were taken with a hand-held electric drill and cut into standard-size (*ca.* 10.5 cc) specimen for palaeomagnetic purpose. Additionally 424 non-oriented samples were taken, of which 408 were drilled and 16 were hand-picked to increase the sampling resolution for chemical analysis. The aim was a minimum sampling resolution of *ca.* 2 kyr for chemical analysis, thus preferably 5 to 6 oriented samples per precession cycle, with additional levels in between each oriented sample for chemical analysis. At the Monte Cardeto subsection the field interpretation yielded a precession cycle of *ca.* 1 m, resulting in spacing between oriented samples of *ca.* 15 – 20 cm. In interval 2a the limestone-marl alternation is twice as thick (*ca.* 2 m), but the resolution is kept constant, since tentative hypotheses such as rapidly changing sedimentation rate or obliquity dominated records could not be (dis)proven in the field. Consequently, one oriented sample was taken on average every *ca.* 18 cm throughout the Monte Cardeto subsection (with 271 oriented samples, field code “SCA”) and Spiaggia della Scalaccia subsection (134 oriented samples, field code “ALS”).

4.1 Palaeomagnetism and rock magnetism

The least weathered specimens of the 405 samples are thermally demagnetized in a magnetically shielded, laboratory-build furnace. NRM (Natural Remanent Magnetization) results of research at younger sections [*Hüsing et al.*, 2009a, 2010] show that the signal is carried by greigite. The samples are heated and measured at 20, 100, 150 and 180°C, followed by 20°C increment steps up to 300°C and the two highest steps at 330 and 360°C.

The NRM is measured on a horizontal 2G Enterprises magnetometer with three DC SQUIDS (noise level 3×10^{-12} Am²). Using principal component analysis the directions of the NRM components are calculated and plotted [*Zijderveld*, 1967; *Kirschvink*, 1980].

16 samples of all lithologies of both subsections are analysed for their magnetic properties using a highly sensitive modified horizontal translation type Curie Balance (instrumental noise level *ca.* 5×10^{-9} Am²) [*Mullender et al.*, 1993] and by the generation of IRM (Isothermal Remanent Magnetization) acquisition curves.

The Curie Balance heats the crushed sample in air with an oscillating field between 150 and 300 mT. The heating starts at room temperature and continues up to 720°C with a heating rate of 5°C/minute and a cooling rate of 10°C/minute. Cooling-heating cycles at discreet temperature steps are used to distinguish thermal behaviour from chemical alteration [*Hüsing et al.*, 2009a]. Therefore cooling-heating cycles of 50°C are applied at 280, 350, 450 and 500°C and one cycle of 70°C at 620°C. After being heated to 720°C, the samples are cooled back to room temperature.

For the generation of IRM acquisition curves the samples are demagnetized by applying a 300 mT field, so these samples are in AF demagnetized starting state [*Heslop et al.*, 2004]. In 61 steps the samples are subjected to a field of 700 mT and the resulting IRM is determined on a robotized SQUID magnetometer (noise level $1-2 \times 10^{-12}$ Am²). The output data is corrected for the sample holder intensity by subtracting the magnetization at 0 mT, which also includes the residual remanence of a sample when it has been demagnetized at 300 mT.

Each IRM curve is then split up in several CLG (Cumulative Log-Gaussian) curves by using component analysis [*Kruiver et al.*, 2001]. Each of those CLG can be characterized by a combination of DP (dispersion parameter), B_{1/2} (mean coercivity) and SIRM (saturation IRM) [*Robertson and France*, 1994].

4.2 Proxies

The specific magnetic susceptibility (m^3/kg) of the 405 primary, non-heated samples is determined by dividing the magnetic susceptibility by the weight of each sample. The magnetic susceptibility is measured on a Kappabridge KLY-2 and the weight on a Sartorius RC 210 P.

Colour measurements of the wet, primary samples are done with a KONICA MINOLTA CM-600d spectrophotometer, resulting in L^* , a^* , b^* (all measured using CIE Standard Illuminant D65) and wavelengths between 400 and 700 nm with a pitch of 10 nm. L^* , a^* and b^* combined a three-dimensional colour model, with L^* representing the black (0) to white (100) scale; a^* the green (negative values) to magenta (positive) scale and b^* represents the blue (negative values) to yellow (positive) scale. To correct for the heterogeneity of each sample, the average of four spot measurements is taken.

64 samples, evenly distributed throughout the subsections, are used for bulk carbon and oxygen isotope analysis. After crushing bulk samples and heating them to 50°C for roughly 24 hours, the samples are measured on SIRA-24 vacuum generators at University Utrecht. The results are corrected with in-house standard NAXOS (25-125 μm ; validated with NBS-18 and -19) and the international IAEA-CO-1 standard.

For the chemical analysis a NITON XL3t 900Analyzer with GOLDD Technology is placed in a Thermo Scientific portable test stand. All primary and non-oriented samples are measured in Cu/Zn Mining Mode (Filters: Main 30, Low 30, High 30 and Light 60 seconds), with on average every 5 samples a control sample (NIST2780). These settings result in an analysis for the following elements: P, Zr, Sr, Fe, Al, Ca, Ti, Ba, Si, Mg, K, Sn, Cd, Pd, Ag, Mo, Nb, Rb, Bi, As, Se, Au, Pb, W, Zn, Cu, Ni, Co, Mn, Cr, V, Sb, Cl and S. For the detection of the lightest elements (Mg, Al, Si, P, S) a helium purge is used. A correction has been applied because of a large discrepancy in the measurements. The differences in the NIST2780 control sample (which is assumed to be homogeneous) are calculated and the resulting difference is added to each measurement.

To correct for the heterogeneity of each sample, three measurements at different spots are averaged to reduce possible errors. A measurement is rejected and then repeated if the standard deviation of that measurement is too large relative to the actual measured value (>1.5 times 2σ).

CaCO_3 content can be determined by multiplying the Ca concentration with the factor 2.496, under the assumption that the entire Ca concentration is bonded to carbonate. Most elements are normalized against Al, since Al is an estimate of the terrigenous input in a marine domain and it is normally not labile in diagenesis [Kruiver *et al.*, 2001]

4.3 Statistics

Spectral analysis is performed in the Analyseries program [Paillard *et al.*, 1996] with the Blackman-Tukey method [Blackman and Tukey, 1958] and a Bartlett window [Bartlett, 1950] applied for the power spectra, including the 80% confidence interval. Using linear interpolation between and extrapolation beyond the magnetostratigraphic tie points the depth records are transformed into records in time, calculated by the Analyseries program [Paillard *et al.*, 1996].

In the online wavelet analysis tool [Torrence and Compo, 1998] a Morlet wavelet is used to generate the wavelet plot. For ω_0 (nondimensional frequency) 6 is used, which is suitable for the admissibility condition [Farge, 1992 and references therein].

5. Magnetostatigraphy

In the younger Monte dei Corvi and La Vedova sections [Hüsing *et al.*, 2007, 2009b] greigite is the main magnetic remanence carrier and so it is plausible that at the Monte Cardeto and Spiaggia della Scalaccia sections greigite is also the main magnetic remanence carrier. This hypothesis is tested by measuring IRM acquisition and by the generation of magnetization versus temperature curves, which is followed by thermal demagnetization to interpret the direction of the characteristic remanent magnetization (ChRM).

5.1 IRM results

Four components have to be introduced in order to achieve a good fit with each IRM curve (see Figure 3). Component 1 is required to fit the low field interval with a mean coercivity, $B_{1/2}$, between 3.98 and 10 mT (see table 1). This fit is similar to that of the Monte dei Corvi and La Vedova IRM acquisition curves [Hüsing *et al.*, 2007, 2009b]. This component is therefore considered to represent thermal activation and can be seen as physically meaningless [e.g. Heslop *et al.*, 2004].

The second is characterized by $B_{1/2}$ values ranging between 45.7 to 63.1 mT and Dispersion Parameter (DP) values between 0.25 and 0.31 \log_{10} mT. Component 3 is characterised by similar $B_{1/2}$ values (between 39.8 and 56.2 mT) as component 2, but the $B_{1/2}$ of component 3 is always lower than the $B_{1/2}$ of component 2. Furthermore, the DP values of component 3 are higher, ranging between 0.37 and 0.47 \log_{10} mT.

The $B_{1/2}$ values suggest that both components are iron sulphides, either greigite or pyrrhotite [Roberts, 1995; Vasiliev *et al.*, 2008; Hüsing *et al.*, 2009a]. The DP values indicate a relatively wide grain size distribution and since component 3 is characterized by higher DP values than component 2, the distribution of grain sizes in component 3 will be wider than in component 2.

Vasiliev *et al.* (2007) and Hüsing *et al.* (2009a) showed that similar $B_{1/2}$ values (between 50 and 65 mT) combined with a low DP (0.19-0.25 \log_{10} mT) are indicative for magnetotactic greigite, however the DP values of component 2 in MCSS are too high to fit in this interval. Therefore it cannot be excluded that magnetotactic greigite is included in component 2.

Component 3 has a very wide DP and therefore it can be explained by authigenic precipitation or growth of greigite. Greigite can precipitate or grow by (inorganic) sulphidization processes, as long as reducing conditions are present in the sediment.

On the other hand, it is also possible that the components 2 and 3 are actually one component with a skewed normal distribution. The generation of CLG curves by component analysis of Kruiver *et al.* (2001) requires Gaussian distributions and therefore two different components have to be introduced to approximate the skewed normal distribution. Based on the IRM results presented here, it is not possible to distinguish between the two hypotheses.

The author prefers the hypothesis with two different greigite components, because of the large differences in the DP values of SCA228 (see Figure 3 and table 1). These two DP values are likely to represent two different greigite populations, because component 2 has a relatively small DP (therefore a narrow grain size distribution), while component 3 is characterised by a high DP (and consequently a wide grain size distribution).

Component 4 is fitted in the high field interval, with $B_{1/2}$ of 288 to 891 mT and DPs between 0.13 and 0.34 \log_{10} mT. It is especially visible in the Standardised Acquisition Plots (SAPs), where its presence causes a “tail” and non-saturation of IRM curves [Kruiver *et al.*, 2001]. This component could be either goethite or haematite; however the weak magnetization (see Figure 4) excludes the presence of haematite. Goethite is more likely present, since it is also a product of weathering [e.g. Kruiver *et al.*, 2001]. Non-saturation of goethite at 700 mT is likely to explain the wide range of $B_{1/2}$ values in this fourth component.

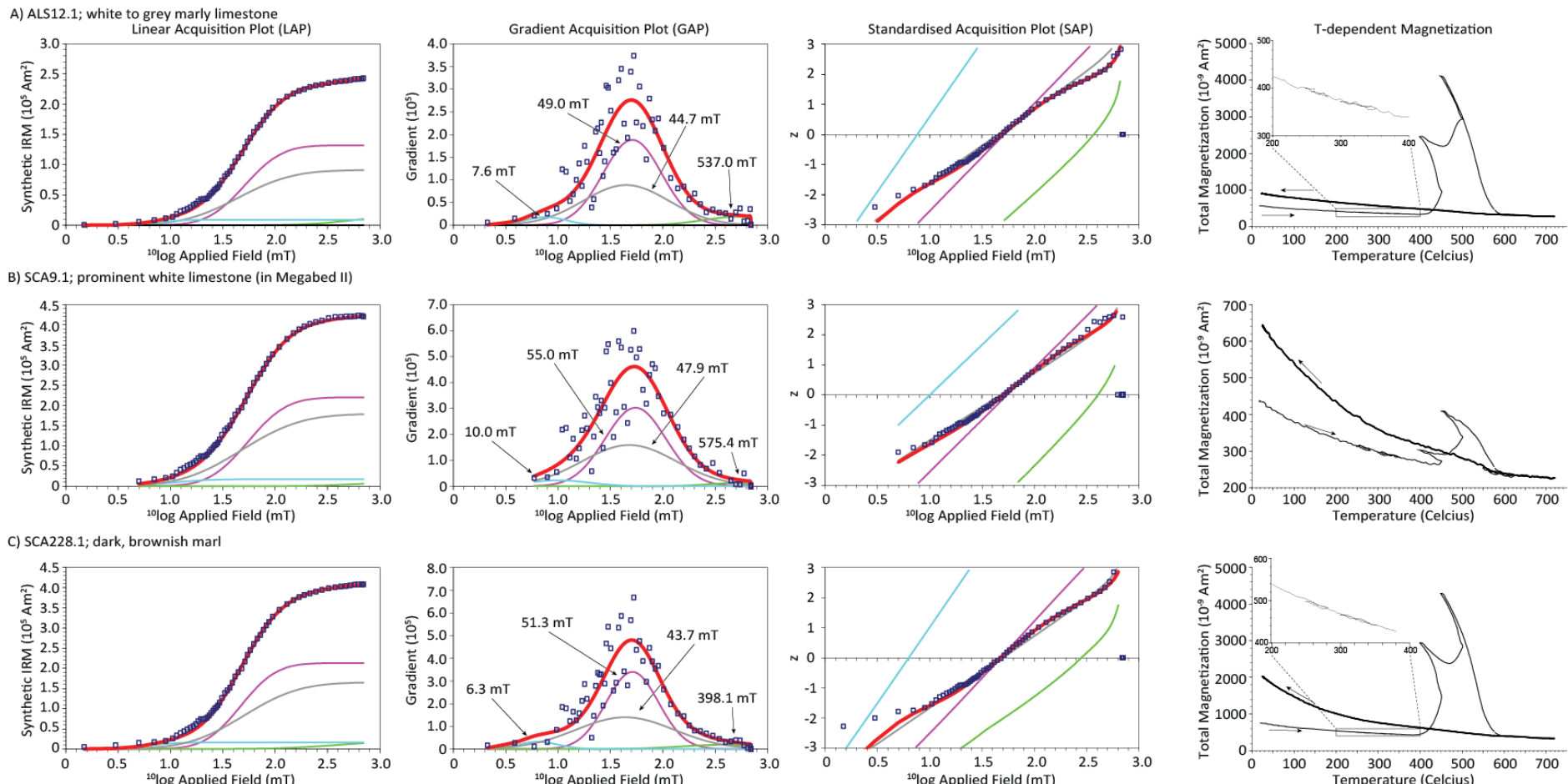


Figure 3: Three representative samples from different lithologies are plotted. The diagrams in the upper row correspond to a whitish-greyish limestone (sample ALS12); the middle row to a prominent whitish limestone in a Megabed (sample SCA9) and the lower row is a dark, brownish marl (sample SCA228). The first three columns from the left are part of the IRM acquisition curves, in which the four components can be recognized. On the left the Linear Acquisition Plot (LAP) is plotted, the middle column of the group of three is the Gradient Acquisition Plot (GAP) with the mean coercivities indicated and the right of those three is the Standardized Acquisition Plot. On the right plots of the thermomagnetic runs are presented, with in the lower and upper one an additional plot with the cooling-heating cycles at 280 and 350°C.

Table 1: The Synthetic Isothermal Remanent Magnetization (SIRM in Am²), mean coercivity (B_{1/2} in mT), Dispersion Parameter (DP in log₁₀ mT) and the relative Contr. (contribution in %) of the SIRM of each component to the SIRM sum. Component 1 is interpreted as thermal activation and therefore physically meaningless; component 2 and 3 as greigite; component 4 as goethite and likely a product of weathering. See text for discussion.

Sample	Component 1 Thermal activation				Component 2 Greigite - 1				Component 3 Greigite - 2				Component 4 Goethite			
	SIRM (Am ²)	B _{1/2} (mT)	DP (log ₁₀ mT)	Contr. (%)	SIRM (Am ²)	B _{1/2} (mT)	DP (log ₁₀ mT)	Contr. (%)	SIRM (Am ²)	B _{1/2} (mT)	DP (log ₁₀ mT)	Contr. (%)	SIRM (Am ²)	B _{1/2} (mT)	DP (log ₁₀ mT)	Contr. (%)
SCA9	1.70E+04	10.0	0.30	4	2.20E+05	55.0	0.29	52	1.79E+05	47.9	0.45	42	1.00E+04	575.4	0.30	2
SCA22	8.00E+03	6.3	0.30	1	4.63E+05	46.8	0.29	58	2.90E+05	39.8	0.43	36	4.00E+04	501.2	0.30	5
SCA46	9.00E+03	6.3	0.30	5	8.05E+04	56.2	0.29	41	9.90E+04	50.1	0.46	50	1.00E+04	794.3	0.27	5
SCA86	1.40E+04	6.3	0.30	3	2.00E+05	52.5	0.28	45	2.00E+05	51.3	0.45	45	3.00E+04	891.3	0.15	7
SCA119	1.60E+04	10.0	0.30	5	1.55E+05	55.0	0.30	49	1.30E+05	43.7	0.44	41	1.70E+04	562.3	0.30	5
SCA162	1.10E+04	7.9	0.30	3	1.60E+05	63.1	0.30	45	1.72E+05	56.2	0.47	49	1.00E+04	741.3	0.13	3
SCA189	1.50E+04	4.0	0.30	3	2.76E+05	50.1	0.26	50	2.30E+05	43.7	0.44	42	2.80E+04	288.4	0.32	5
SCA209	2.00E+04	7.9	0.30	6	1.30E+05	56.2	0.27	36	2.00E+05	50.1	0.43	55	1.25E+04	707.9	0.20	3
SCA228	1.60E+04	6.3	0.20	4	2.13E+05	51.3	0.25	51	1.65E+05	43.7	0.47	40	2.00E+04	398.1	0.42	5
SCA259	6.00E+03	5.0	0.30	3	1.22E+05	51.3	0.28	52	9.70E+04	49.0	0.43	41	9.00E+03	316.2	0.15	4
ALS12	9.00E+03	7.6	0.20	4	1.32E+05	49.0	0.28	53	9.10E+04	44.7	0.41	37	1.60E+04	537.0	0.34	6
ALS23	1.00E+04	10.0	0.20	3	1.13E+05	52.5	0.25	34	1.83E+05	39.8	0.39	54	3.00E+04	562.3	0.30	9
ALS48	1.60E+04	7.9	0.20	8	7.50E+04	55.0	0.27	39	8.10E+04	49.0	0.37	42	2.20E+04	501.2	0.25	11
ALS82	3.00E+03	5.6	0.22	2	4.85E+04	50.1	0.28	37	7.25E+04	44.7	0.44	55	8.00E+03	631.0	0.25	6
ALS90BC	6.00E+03	5.0	0.23	3	1.27E+05	49.0	0.31	54	8.50E+04	45.7	0.44	36	1.60E+04	776.2	0.15	7
ALS94					1.22E+05	51.3	0.29	54	9.10E+04	46.8	0.47	40	1.30E+04	398.1	0.34	6

5.2 Results of thermomagnetic runs

All 16 thermomagnetic runs show similar thermal behaviour, which is an indication that the carrier does not change with lithology. In Figure 3 three representative examples are shown, where ALS12 is a white to grey marly limestone, SCA9 is an indurated white limestone of Megabed II and SCA228 is a dark, brownish marl. The maximum value of total magnetization is always higher in the marls than in the limestones.

In all three examples there is a general hyperbolic decrease in total magnetization up to 280°C, where the first cooling-heating cycle is present. SCA228 (dark, brownish marl) (see Figure 3, row C) shows a small decrease in total magnetization during the cooling step in this cooling-heating cycle, indicating that an irreversible process is occurring here. In ALS12 and SCA9 (Figure 3, respectively row A and B) this small decrease might be present, but because of the very low total magnetization and the noisiness of the data, this remains uncertain. In the second cooling step (from 350 to 300°C) a similar decrease might be visible in all three diagrams, but because the very low total magnetization and the noisiness of the data this is unclear.

At 420°C, there is a rapid increase in total magnetization in all samples, but the amplitude of this increase is much larger in ALS12 and SCA228 than in SCA9. In the cooling step of the next cooling-heating cycle (from 450 to 400°C), the total magnetization continues to increase and decreases in the heating phase of this cycle. The increase of total magnetization during cooling is also present in the following cooling-heating cycle (from 500 to 450°C), followed by a rapid decrease in total magnetization to 590°C. When the samples are heated from 590°C to 720°C there is a gradual decrease in the total magnetization. From 720°C the samples are cooled back to room temperature. The total magnetization of the cooling curve follows the heating curve up to 590°C. The heating curves showed a large increase between 420 and 590°C, but the cooling curve shows a slow increase in total magnetization in this interval. At ca. 400°C, the total magnetization of the cooling curve is higher than the total magnetization of the heating curve (which starts to increase at ca. 420 at ca. 400°C). From ca. 400°C to room temperature the total magnetization increases in a hyperbolic shape and remains higher than the total magnetization of the heating curve.

The described patterns are indicative of several iron sulphides. In the relatively low temperature interval (up to ca. 360°C), the irreversible cooling-heating cycle (250 to 280°C) in SCA228 is indicative for greigite [Vasiliev *et al.*, 2007, 2008; Hüsing *et al.*, 2009a]. In ALS12 and SCA9 this irreversible step is not as clearly visible, because the low magnetization and noisiness of the data.

The second cooling-heating (300 to 350°C) does not show the characteristic irreversible pattern and is then caused by paramagnetism [e.g. Passier *et al.*, 2001]. On the other hand, the irreversible step might be present, but cannot be observed because of low magnetization and the noisiness of the data. This would be again an indication for greigite (although uncertain), which is supported by the IRM results.

The large increase in magnetization at ca. 420°C is indicative for the oxidation of pyrite [Krs *et al.*, 1992]. As can be expected, the pure limestone bed (SCA9 from Megabed II) will consequently contain less pyrite than the marls or marly limestones. The oxidized pyrite is removed at ca. 590°C, it is likely that this iron oxide is magnetite (Curie temperature is 580°C). When the cooling from 720°C to room temperature starts, the increase in total magnetization might be explained by the formation of superparamagnetic iron oxides at higher temperatures [Passier *et al.*, 2001].

5.3 Palaeomagnetism

At room temperature the NRM is very low (it varies between 0.0007 and 0.0328 mA/m), but a significant part (73%) of the samples is considered reliable in order to plot the magnetostratigraphic pattern. Four Zijderveld diagrams from MCSS [Zijderveld, 1967] are presented containing three different components (called components A to C) when thermally demagnetized (see Figure 4). Component A is present at low temperatures (up to 100°C) and is characterised by a random orientation. Component B is present up to 180 to 200°C and is also randomly oriented, but not in the same direction as component A. Component B ends with a cluster of several measurements (from ca. 180-200°C, up to 240°C) and this cluster is the start of component C. This component C decreases

from the cluster towards the origin and ends with a randomly oriented in NRM intensity, often occurring at 300–330°C, although some samples show an increase at already 280°C or later at 360°C. Component A and B are interpreted as overprints, since their directions are random. The clusters and decrease in intensity of component C are present in both reversed and normal polarity and therefore this component C is considered to be the primary component.

In Figure 4 all ChRM directions of component C are plotted in an equal area plot, revealing a slight non-antipodality between the normal and reverse directions. A non-antipodality has also been found in the younger sections [Hüsing *et al.*, 2010; Mourik *et al.*, 2010], which is explained by overlapping blocking temperatures of the components. Overlapping blocking temperatures are likely to cause the non-antipodality also in this research, since it is plausible that all three components recognised in the Zijderveld diagrams (Figure 4) might be carried by greigite (Figure 3). Even though the ChRM directions are not perfectly antipodal, there are two distinct clusters of normal and reversed samples and these directions are considered reliable for a magnetostratigraphic plot.

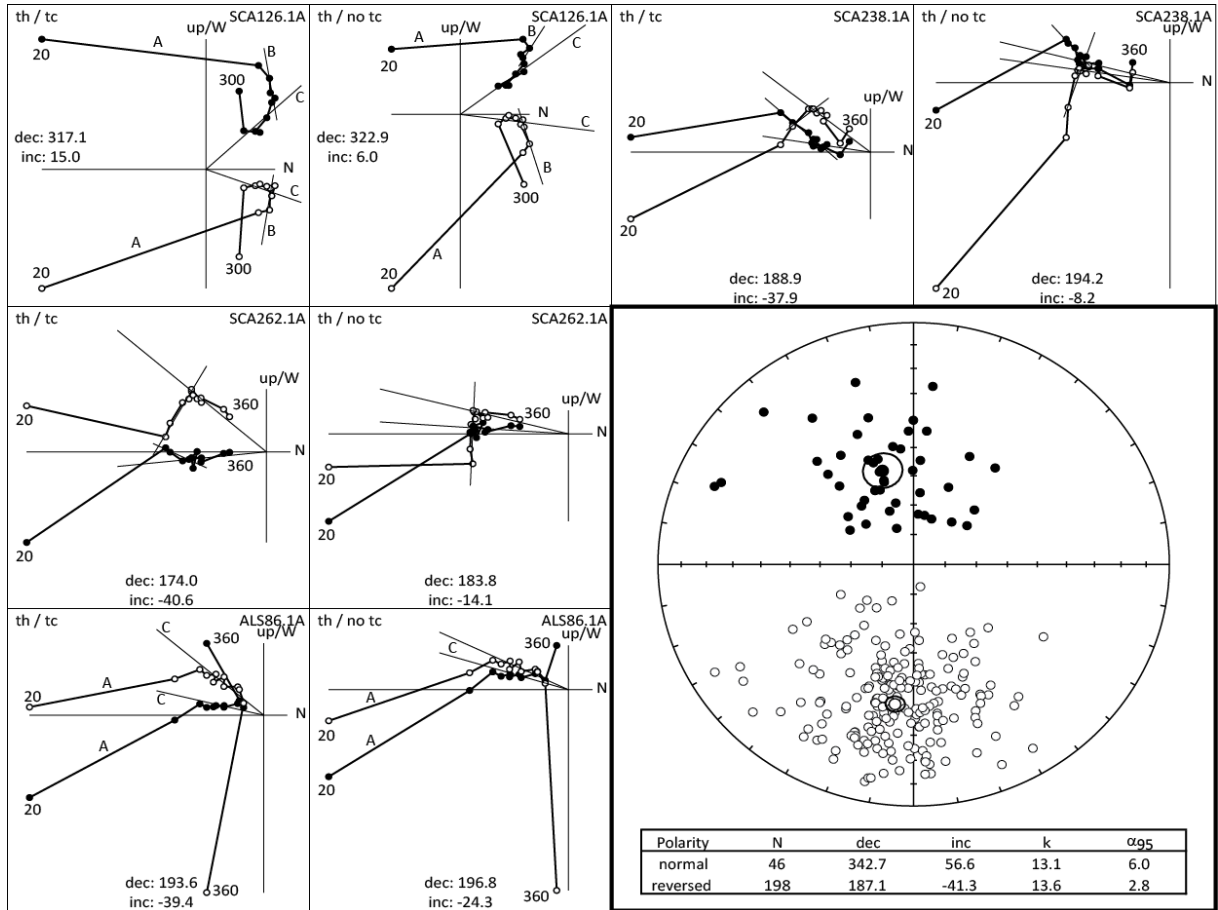


Figure 4: Four representative Zijderveld diagrams are plotted with (tc) and without (no tc) tectonic correction. All samples are thermally demagnetized. In SCA126 (upper left corner of diagram) the three components (A to C) are indicated and in ALS86 (lower left corner of diagram) B is not identified and consequently only A and C are indicated. Upper right corner is sample SCA238 and middle left diagrams are sample SCA262. Several temperature steps are indicated next to the measurements. In the lower right corner all ChRM directions of component C are plotted in a stereonet, indicating a slight non-antipodality. The amount of samples (N) sorted per polarity (either normal or reversed) are indicated with an average declination (dec) and inclination (inc), Fisher's precision parameter k and the radius of the 95% confidence cone (α_{95}). See text for discussion.

By plotting all ChRM directions of component C are in stratigraphic order (see Figure 5), three relatively short normal polarity zones are present in the upper half of the section. The lower half of the section (<45 m) is characterised by reverse polarity only. Despite the high sampling resolution, the uncertainties around the reversals are generally large (uncertainty ranging between 1.88 m and 2.77 m), except for the upper reversal, with an uncertainty of 0.51 m. These uncertainty intervals are

characterized by low quality Zijderveld Diagrams and samples with transitional or unusual combinations of declination and inclination angles. Some of this might be explained by the fact that the Earth's magnetic field can take up to 10 kyr (as recorded in sediments) to reverse [Clement, 2004].

Following the correlation of the La Vedova section [Turco et al., 2011], which recorded the C5Cn.1n/C5Br reversal at ca. 16 m, the uppermost subchron in MCSS is C5Cn.1n. Continuing downwards, the normal polarity zone in UDL (Upper Double Limestone at ca. 60 m) is C5Cn.2n and the lowest normal at 46-52 m correlates to C5Cn.3n. The long reverse polarity interval in the lower half of the section is consequently C5Cr.

Using the GTS2012 ages [Hilgen et al., 2012] of the reversal boundaries, a first order age model can be plotted (Figure 5) and the corresponding sedimentation rate can be calculated. This age model assumes constant sedimentation rate between the calibration points (reversal boundaries). This results in different sedimentation rates for the individual subchrons in C5Cn (from 3.0 to 18.6 cm/kyr). On average the sedimentation rate is 5.5 cm/kyr (4.5 cm/kyr if the exceptionally high C5Cn.1r is excluded) and therefore a hypothetical sedimentation rate of 5 cm/kyr is extrapolated towards the base of the section (see Figure 5).

A significant implication of this interpolation is that an additional reversal boundary (top of C5Dn) would be expected to be recorded in the lower part of the section. However, there is no indication in the palaeomagnetic data for normal polarity in the lower meters, but instead all samples have a reliable reverse polarity. Therefore a second hypothetical sedimentation rate of 10 cm/kyr is plotted. The position of the C5Dn-C5Cr reversal is now expected to be about -5 m (below the base of the here presented section).

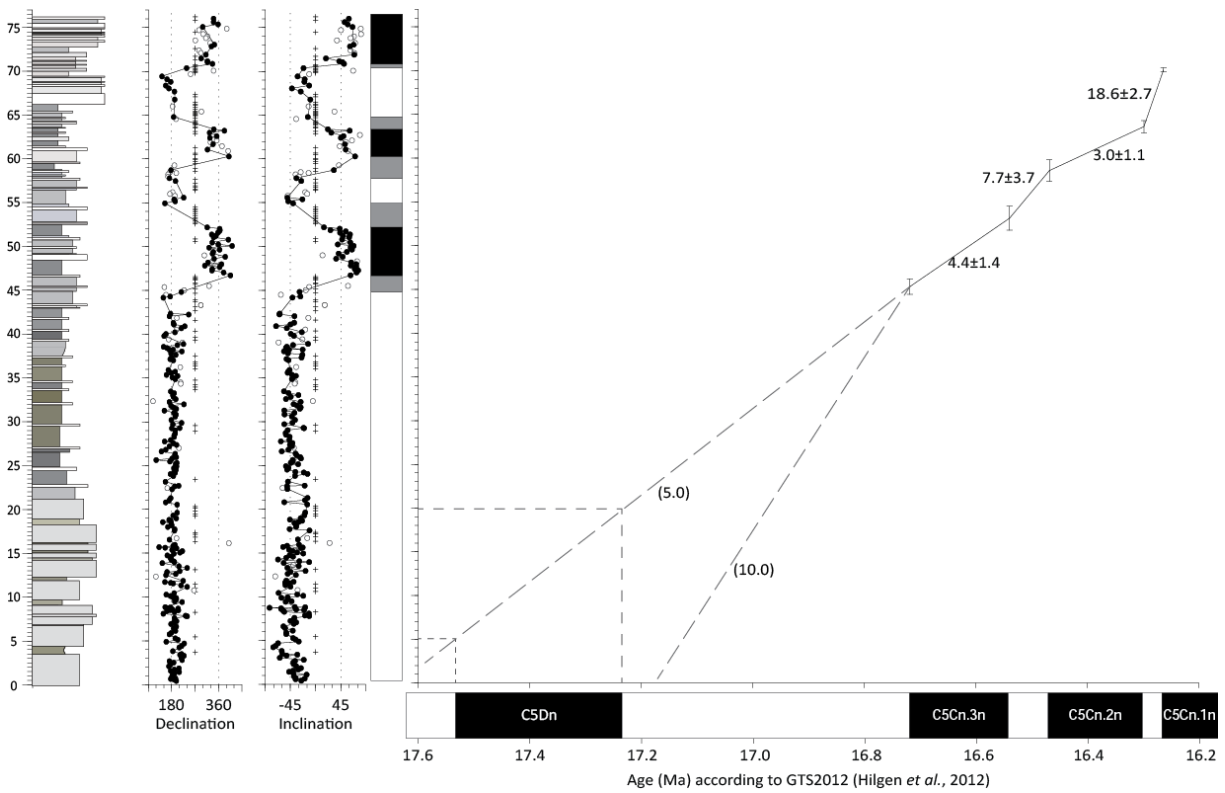


Figure 5: The stratigraphic log is plotted with the certain (closed dots), uncertain (open dots) and unreliable (crosses) ChRM directions of component C and the corresponding normal (black) or reversed (white) polarity. The grey interval indicates the uncertainty of the reversal interval. Interpolation between the GTS2012 [Hilgen et al., 2012] reversal ages is used to calculate the sedimentation rate (in cm/kyr), including errors corresponding to the uncertainties around a reversal. For the lower half of the section two hypothetical sedimentation rates (5 and 10 cm/kyr) are plotted and the corresponding hypothetical ages of the sediment.

6. Proxies

6.1 Magnetic susceptibility

The earlier subdivided lithological intervals 1 to 3 are also characterized by different values for the specific magnetic susceptibility (see Figure 2). In interval 1 the specific magnetic susceptibility varies from 1.09×10^{-8} to $3.06 \times 10^{-8} \text{ m}^3/\text{kg}$ and averages at $2.02 \times 10^{-8} \text{ m}^3/\text{kg}$. The higher values are reached in the marl at *ca.* 4, 18.5 and 21 m, whereas the lower values are present in the limestones (e.g. the prominent limestone bed at *ca.* 8 m) and the more prominent intervals “D” and “E”.

In interval 2a the lower values are also present in the limestones and the higher values in the marls, but the main difference with interval 1 is the value and amplitude of the specific magnetic susceptibility: it varies from 1.82×10^{-8} to $4.12 \times 10^{-8} \text{ m}^3/\text{kg}$ and gradually increases to an average of $3.12 \times 10^{-8} \text{ m}^3/\text{kg}$, which is significantly higher than in interval 1. The greyish marl at *ca.* 39 m is characterised by unusually low values of specific magnetic susceptibility (relative to the surrounding marls).

Interval 2b has similar values, but the average is slightly lower ($2.97 \times 10^{-8} \text{ m}^3/\text{kg}$) and the amplitude of variations is slightly larger than in interval 2a (ranging from 1.55×10^{-8} to $4.49 \times 10^{-8} \text{ m}^3/\text{kg}$). The six darker marls (“a” to “f”) have the highest maxima and the limestone-rich beds (double and triple limestones) are characterised by lower values.

From interval 2b to 3 there is a sharp decrease of specific magnetic susceptibility, resulting in values more similar to interval 1, with an average of $2.10 \times 10^{-8} \text{ m}^3/\text{kg}$ ($1.79 \times 10^{-8} \text{ m}^3/\text{kg}$ in the Megabeds; $2.49 \times 10^{-8} \text{ m}^3/\text{kg}$ in the marly interval in between), ranging between 0.78×10^{-8} and $3.12 \times 10^{-8} \text{ m}^3/\text{kg}$. The highest values are still present in the marls, whereas the lowest values are in the limestones of the Megabeds.

6.2 Colour

The dimensionless grey scale L*(D65) from black (0) to white (100) of interval 1 varies from 35.2 to 51.9, with an average value of 42 (see Figure 2). The L* record of interval 1 shows a repetitive pattern varying between *ca.* 36 and 50 with peaks every *ca.* 3 m up to *ca.* 16 m and one *ca.* 4 m repetition between *ca.* 16 and 20 m. Only at the base of “E” the minimum remains closer to the average L* values, thus lighter than the other minima. The top of “E” is characterised by low (35.2, so dark grey) L* values. In general the higher (whiter) values are present in the more indurated, grey marly limestones of interval 1 and the darker colours in the intervals with brownish marls.

From interval 1 to interval 2a there is an amplitude increase in L* to the highest (whitest) values (61.5) of the entire section in the limestone bed at *ca.* 22.5 m. The marl on top of this limestone is – as expected – darker, with L* 39.8. This light limestone-dark marl alternation repeats throughout the entire interval 2a (ranging from 37.6 to 61.5 with an average of 44.8). The relative prominence (as indicated with f, n, d and p in Figure 2) matches very well with the values for L*. The highest numbers in L* (thus more whitish) are in the well pronounced white limestones, whereas the decreasing numbers of L* in the maxima corresponds very well with the decreasing degree of prominence of the limestones, thus becoming more grey. Surprisingly the indurated, grey marl at *ca.* 39 m is not much lighter than the surrounding marls, which is expected based on the weathering colour.

No significant difference between interval 2a and 2b is visible in the L* record, since there is no change in values or pattern around *ca.* 43 m. L* continues to vary between 36.9 and 57.8 with an average of 44.5, very similar to the values of interval 2a. The phase relation of high (light) values for limestones and low (dark) values in marls is present, although the prominent marls in the double/triple limestones are not much lighter (higher values) than the marls “a” to “f”, which were logged as dark.

From the top of interval 2b to interval 3 there is a rapid increase in L* (whiter grey) from 40.4 in the marl to 53.1 at the base of Megabed I, which also supports the lithological division between interval 2b and 3. In interval 3 the L* values are on average slightly higher (47.2) than in interval 2b (average 44.5), but the variations in amplitude are reduced (L* varies between 41.6 and 54.6). The three-point moving average seems to follow the overall induration pattern related to the two Megabeds separated by a less indurated dark marly interval.

6.3 Bulk isotopes

In interval 1 the bulk $\delta^{13}\text{C}$ record has maxima (“heavy” ratio of 0.8-0.85‰ VPDB) at *ca.* 1 and 10-15 m with a minimum between *ca.* 4 and 7 m of -0.059 to 0.095‰ (see Figure 2). After the maximum at *ca.* 15 m, the ratio gradually decreases (lighter ratio) into interval 2a, with the minimum of -0.04‰ at *ca.* 28.5 m. A rapid decrease of 0.75‰ is present between 32 and 34 m, reaching the lowest ratio of -0.57‰. After a small increase of *ca.* -0.2‰, the minimum in the $\delta^{13}\text{C}$ record ends at *ca.* 41 m with a rapid increase from -0.48‰ to 0.82‰ at *ca.* 45 m. This increase corresponds to the change from interval 2a to 2b.

Interval 2b is characterised by three high amplitude maxima (0.4-0.7‰ increase, up to 1.06‰) at *ca.* 45, 49 and 57 m and two low amplitude maxima (0.3‰ increase to 0.44‰) at *ca.* 53 and 63 m. The minima vary between 0.1 and 0.3‰ and the $\delta^{13}\text{C}$ record averages 0.45‰. From interval 2b to interval 3 the $\delta^{13}\text{C}$ increases gradually to a maximum ratio of 1.01‰ in Megabed I and 0.94‰ in Megabed II. The $\delta^{13}\text{C}$ drops to 0.24‰ in the marls in between the Megabeds, so the ratios of interval 3 are similar to interval 2b and the lithological division cannot be observed in the $\delta^{13}\text{C}$ record. In interval 2b and 3 the maxima in $\delta^{13}\text{C}$ are in general correlated to the more prominent beds, while in interval 1 only “E” can be correlated to a $\delta^{13}\text{C}$ maximum.

The bulk $\delta^{18}\text{O}$ record of interval 1 is characterised by a double maximum between *ca.* 8 and 15 m (ranging -0.58 to -0.28‰ VPDB), preceded by a minimum of -1.08‰ at *ca.* 4 m (see Figure 2). After the double maximum the $\delta^{18}\text{O}$ decreases to -1.24‰ at *ca.* 27 m (already in interval 2a), with one increase of 0.4‰ (from -0.94‰ to -0.54‰) between *ca.* 18.5 and 20.5 m. The maxima in the bulk $\delta^{18}\text{O}$ record correlate to the more prominent parts of interval 1 (especially at *ca.* 8, 15 and 20 m).

After the gradual decrease into interval 2a, rapid fluctuations in the bulk $\delta^{18}\text{O}$ record occur. Between *ca.* 27 and 40 m $\delta^{18}\text{O}$ varies between -1.60 and -0.77‰, while the average remains roughly -1.1‰. At *ca.* 46 m, at a comparable position as the $\delta^{13}\text{C}$ record, there is a rapid increase to -0.60‰. This increase coincides with the change from interval 2a to 2b.

After the maximum at *ca.* 46 m the bulk $\delta^{18}\text{O}$ returns to an average of -1.1‰ (similar to the average of interval 2a), with again rapid fluctuations between -1.4‰ and -0.9‰ (with one negative exception of -1.6‰ at *ca.* 52 m) up to 59 m. The onset of interval 3 is characterised by a slow decrease from -0.97‰ at 59 m to -1.28‰ at 63 m, followed by an increase peaking at -0.78‰ in Megabed I.

The characteristic change from interval 2b to interval 3 cannot be recognised in the $\delta^{18}\text{O}$ record. Furthermore, the two Megabeds are not present as individual maxima or minima in $\delta^{18}\text{O}$, since the lowest $\delta^{18}\text{O}$ of interval 3 is present at the base of Megabed II, but at the same time $\delta^{18}\text{O}$ also peaks in the top of Megabed II.

6.4 Chemistry

In Figure 2 the five chemical proxies (CaCO_3 content, Rb/Sr, Ti/Al, Ba/Al and Si/Al) with the most interesting variations throughout the section are plotted. In interval 1 six maxima (ranging between 70 and 80%) are present in CaCO_3 (at *ca.* 3, 5.5, 9, 12.5, 16.5 and 20.5 m), which correlate negatively to Rb/Sr and Si/Al. Compared to the upper part of the section, CaCO_3 experiences relatively small amplitude variations in the interval between *ca.* 7 to 16 m, as well as the Rb/Sr between 0.011 and 0.018, whereas the Si/Al record is characterised by large-scale amplitude variations (between 3.6 and 11.9). This interval is also characterised by an on average lower Ti/Al ratio (<0.03), which correlates negatively to CaCO_3 . In the rest of interval 1 this phase relation is less clear, because of very small amplitude changes in Ti/Al. Ba/Al correlates positively to CaCO_3 , although this phase relation is less clear in the middle part of interval 1, where the lowest ratio of 0.01 is reached.

The prominence of interval 1 seems to be correlated to the Si/Al ratio, which is highest in “D” and “E”. The softer, marly intervals at *ca.* 4, 9.5 and 12.5 m are characterised by large minima in the Si/Al and small scaled minima in Si/Al are present in the three softer less indurated beds at *ca.* 14.5, 15.2 and 16.2 m (in “E”).

A large CaCO_3 maximum (90%) characterises the transition from interval 1 to 2a at *ca.* 22.5 m, present in the first prominent green-greyish limestone. Furthermore, this limestone is characterised

by relatively (for interval 2a) large maxima in Ba/Al and large minima in Rb/Sr, Ti/Al and Si/Al. The phase relation of the ratios in interval 1 continues into interval 2a, although the amplitude of the variations changes, which supports the lithological division of these intervals.

The prominence of the green-greyish limestones seems to fit with the amplitude of the maxima in CaCO₃, since the less prominent limestones in the middle part (*ca.* 33-37 m) of interval 2a are also characterised by lower CaCO₃ content.

The repetitive pattern of maxima of CaCO₃ and Ba/Al and minima of Rb/Sr, Ti/Al and Si/Al in the limestones is present throughout interval 2a. The grey marl at *ca.* 39 m is preceded by an unusually high Ti/Al (up to 0.056) between *ca.* 35 and 37 m and a strong decrease in amplitude of maxima in Rb/Sr (from 0.031 at *ca.* 35 m to 0.025 at *ca.* 37 m). These lower amplitude maxima in Rb/Sr are not uncommon in interval 2a as Rb/Sr <0.027 is also present at *ca.* 28 and 31 m.

A large, rapid increase in Si/Al (from 3.5 to 6.8) and more gradual increase in Ti/Al (from 0.033 to 0.050 between *ca.* 39 and 43 m) characterises the base of interval 2b, in the LTL (Lower Triple Limestone). The phase relation between interval 2a and 2b is similar, since CaCO₃ and Ba/Al still peak in the limestones and Rb/Sr, Ti/Al and Si/Al peak in the marls. The six darker marls ("a"-“f”) are characterised by large amplitude maxima (0.03-0.035) in Rb/Sr, whereas the Rb/Sr maxima of the other marls (except the marl between “a” and “b”) remain at lower amplitude (<0.025). This phase relation is also visible in the CaCO₃ minima, since the lowest concentrations are reached in the dark marls (with the exception of the marl between “a” and “b”).

The Si/Al ratio is characterised by large-scale amplitude changes (relative to interval 2a) with the large-scale maxima in the more prominent parts of interval 2b. The individual marl-limestone alternations result in some short maxima (marls) or minima (limestones) on top of those larger scaled changes. In the dark marl “a” there is a large increase in Si/Al, from 4 to 8, which drops back to 4 in the marl above “a” and then increases again to 8 at the base of Megabed I (and thus interval 3).

The transition from interval 2b to 3 is also characterised by a minimum in Rb/Sr. The amplitude of the variations in Ti/Al and Ba/Al become somewhat smaller, but especially the amplitude variations in CaCO₃ decrease, ranging between 60 and 80% (in interval 2b this was between 40 and >95%). Although the amplitude of the variations decreases, the phase relation remains similar over the transition from interval 2b to interval 3. The maxima in CaCO₃ in the limestones correlate positively to Ba/Al and negatively to Ti/Al, Rb/Sr and Si/Al, although the higher amplitude maxima in the Si/Al record cannot be correlated to the CaCO₃ content. The marly interval intercalated between Megabeds I and II is in general characterised by a lower CaCO₃ and higher Rb/Sr and Ti/Al, although individual limestone beds in this interval have higher CaCO₃ and lower Rb/Sr and Ti/Al.

Based on the research done on the younger sections [Hüsing *et al.*, 2010; Turco *et al.*, 2011] and the constant phase relation between the elements presented here, the marl-limestone alternation might have a common origin and can most likely be used for an astronomical tuning.

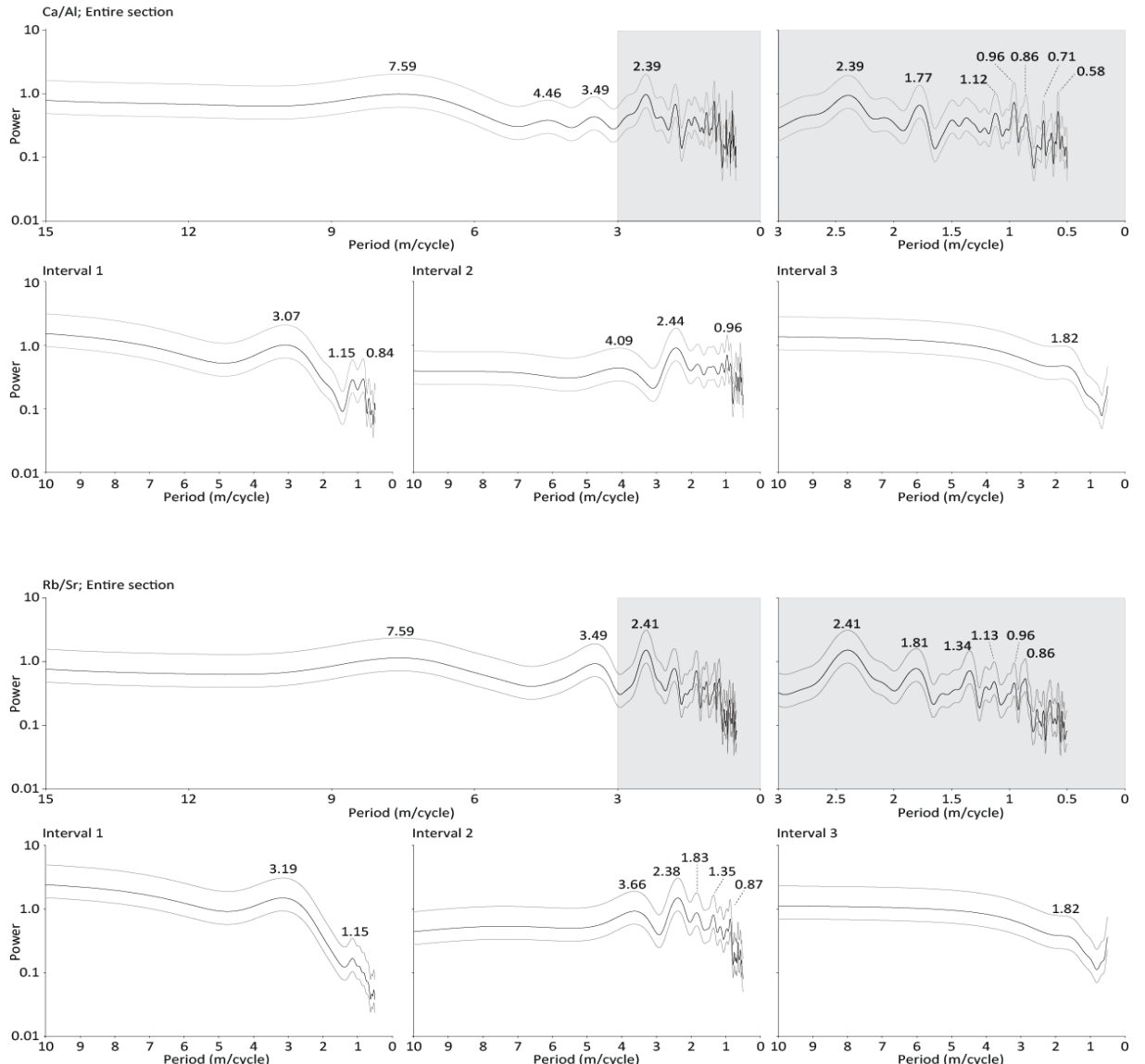


Figure 6: For both the Ca/Al (upper diagrams) and Rb/Sr (lower diagrams) ratios four power spectra are generated (black line) with their 80% confidence (grey lines). The upper two diagrams of both ratios are spectra of the entire section and the grey shaded diagram on the right is an enlargement of the left spectrum. The lower three diagrams are power spectra of single intervals. For all power spectra the period (in m) of the peaks are indicated.

7. Statistics

To check whether the variations in lithology and proxies can be related to the astronomical parameters, the ratios of the cycles found in the section should be close to the ratios between these three parameters (eccentricity:obliquity:precession roughly 1:2.5:5). Ca/Al and Rb/Sr show the best repetitive pattern and are thus the proxies with the most potential to be used in an astronomical tuning.

7.1 Statistics in depth domain

7.1a Spectral analysis

For both the Ca/Al and Rb/Sr record, power spectra (see Figure 6) are generated for the entire section and for the three intervals, because of the differences between the three intervals in appearance (and possibly sedimentation rate). In both Ca/Al and Rb/Sr spectra significant peaks are found with periods of *ca.* 1 m (0.86, 0.96 and 1.12-1.13 m), *ca.* 1.8 m (in Ca/Al 1.77 m; in Rb/Sr 1.81 m) and *ca.* 2.4 m (in Ca/Al 2.39 m; in Rb/Sr 2.41 m). Two peaks with a longer period are present in the Rb/Sr spectrum at *ca.* 3.5 m and *ca.* 7.6 m, although the latter is not significant. Similar non-significant peaks are also present in the Ca/Al spectrum, at *ca.* 3.5, 4.5 and 7.6 m. It seems plausible that the wide peak in the Rb/Sr power spectrum is similar to the two smaller peaks at *ca.* 3.5 and 4.5 m in the Ca/Al spectrum.

In the power spectra of the separate intervals only the *ca.* 2.4 m peak in interval 2 is significant for both Ca/Al and Rb/Sr. The spectra of interval 3 do not show any significant peak, only at *ca.* 1.8 m there is a “flattening” in the plot. Interval 3 is probably too short to be represented by any significant peaks.

All peaks in the power spectra should originate from the record (otherwise they are a mathematical misrepresentation), therefore different filters are applied on the Ca/Al and Rb/Sr records (Figure 7). The longest period (*ca.* 7.6) is not significant, but when the records are filtered between 5.26 and 10.0 m, it shows distinct variations, which can be correlated to the prominence of the lithological log. The two Megabeds and the prominent intervals in interval 2b have maxima in the filtered Ca/Al record and minima in the filtered Rb/Sr record, although difficulties occur at *ca.* 45-55 m, where the one cycle of the filter is relatively thick and might represent a double cycle. This double cycle cannot be observed in Ca/Al, but there is a small amplitude change visible in the Rb/Sr filter.

In the lower half of the record (0-30 m) this long filter does not match the lithological expression anymore and therefore also shorter periods of interval 2 (narrow filters with periods of *ca.* 1, 2.5 and 4 m) are plotted and the dominant period in interval 1 (wide filter, between 1.39 and 5.0 m). The *ca.* 4 m filter of both Ca/Al and Rb/Sr match the marls “a” to “f” and the more prominent intervals (double/triple limestones) in interval 2b and so the *ca.* 3.5-4 m peaks in the power spectra of the entire section and interval 2 originate from these marls.

The *ca.* 2.5 m peak in the entire section spectra of both Ca/Al and Rb/Sr is caused by a combination of peaks in interval 1 and 2a. The dominant cycle in interval 1 is *ca.* 3 m and this cycle can be approximated by applying a filter between 1.39 and 5.0 m. However, some mismatches occur as the amplitudes of the Rb/Sr and Ca/Al records drop and the filter shows some cycles which cannot be observed in the entire dataset. The other part of the *ca.* 2.5 m peak in the entire section spectra is caused by a *ca.* 2.4 m peak, present in both Ca/Al and Rb/Sr. The applied filter matches the record and only in the upper part of interval 2 some mismatches occur when the thickness of the marl-limestone alternation changes.

In the upper part of interval 2a, around the grey marl at *ca.* 39 m, this filter does not match the record anymore, which is expected based on the change of thickness of the dominant marl-limestone alternation from *ca.* 2-2.5 m to *ca.* 1 m in the upper half of interval 2a. For the top of interval 2a and for the entire interval 2b the *ca.* 1 m filter has to be used, but a *ca.* 1 m cycle is not a perfect approximation of the cyclicity in the record (especially in the dark marls, LDL and UDL). The 1 m filter introduces additional (non-observed) cycles in the marls, which might not be there. These possibly (fake-)positives are making the statistical analysis much more difficult, especially by transferring the records from the depth domain into the time domain.

7.1 Wavelet analysis

The shift in the dominant period (*ca.* 1 m in the interval 2b to *ca.* 2-2.5 m in the lower half interval 2a) is clearly visible in the wavelet spectra of Ca/Al and Rb/Sr (Figure 8), since the 1-m period is absent below and present above *ca.* 33 m. The 1 m period is also absent at *ca.* 39, 45 and 55 m, corresponding to thicker marls. In the top of interval 2 the 1 m period seems to be repetitive present and absent every 2-2.5 m, which corresponds to the interval with bundling below the indurated, light grey marl at *ca.* 39 m. At the same time the power of the *ca.* 2-2.5 m period is quite low here, which is quite unexpected because of this bundling. In interval 2b of both Ca/Al and Rb/Sr, at *ca.* 50, 57 and 64 the 1 m period is dominant, which corresponds to the intervals where the 1 m filter (see Figure 7) is also matching best.

In interval 1 and the lower half of interval 2a of both Ca/Al and Rb/Sr the *ca.* 2-2.5 m cycle is present, except at *ca.* 10-17 m, the same interval where the filters showed some difficulties (see Figure 7). In the lower half of interval 1 the period might be closer to *ca.* 3 m instead of *ca.* 2 m, whereas the dominant period in the lower half of interval 2 is closer to *ca.* 2 m. This shift in thickness is a plausible explanation of the wideness of the prominent peak in the power spectrum of interval 1 (see Figure 6).

The shorter periods show an important shift in period from at *ca.* 2-2.5 m to *ca.* 1-1.5 m at *ca.* 30-40 m, but this shift is not clearly present in the longer periods (>3 m) in the wavelets of both Ca/Al and Rb/Sr. In interval a *ca.* 7-8 m period is present and this continues into interval 2a. At the end of interval 2a this period becomes wider and at the base of interval 2b the *ca.* 7-8 m period is not highly dominant anymore. Here a lower period of *ca.* 4 m in interval 2b is present, representing the thicker marls. Between 45 and 55 m (lower part of interval 2b) there is also a *ca.* 10 m period present, instead of the *ca.* 7-8 m of interval 2a. This is probably similar to the relatively thick (double?) cycle in the 5.26-10.0 m filter (see Figure 7). In the upper part of interval 2b the *ca.* 7-8 m period is again more dominant and continues into interval 3. In interval 3 there is not much cyclicity visible, because this record is probably too short to be represented by clear cycles.

Approximate ratios 1:2.5:5 (eccentricity:obliquity:precession) cannot be straightforwardly found in these records. In the upper part of interval 2b the *ca.* 4 m and 6-10 m filters might approximate the 1:2.5 ratio of eccentricity:obliquity, but a period of *ca.* 2 m is not completely representative for interval 2b. On the other hand, the *ca.* 1 m filter is not a perfect representation of the record either and especially in the double limestones (LDL, MDL and UDL) and the lower dark marls ("d" to "f") the period is *ca.* 2 m. Therefore, even though the observed ratio is closer to *ca.* 1:2:4, instead of *ca.* 1:2.5:5, the astronomical variations might be forcing the alternations present in this record.

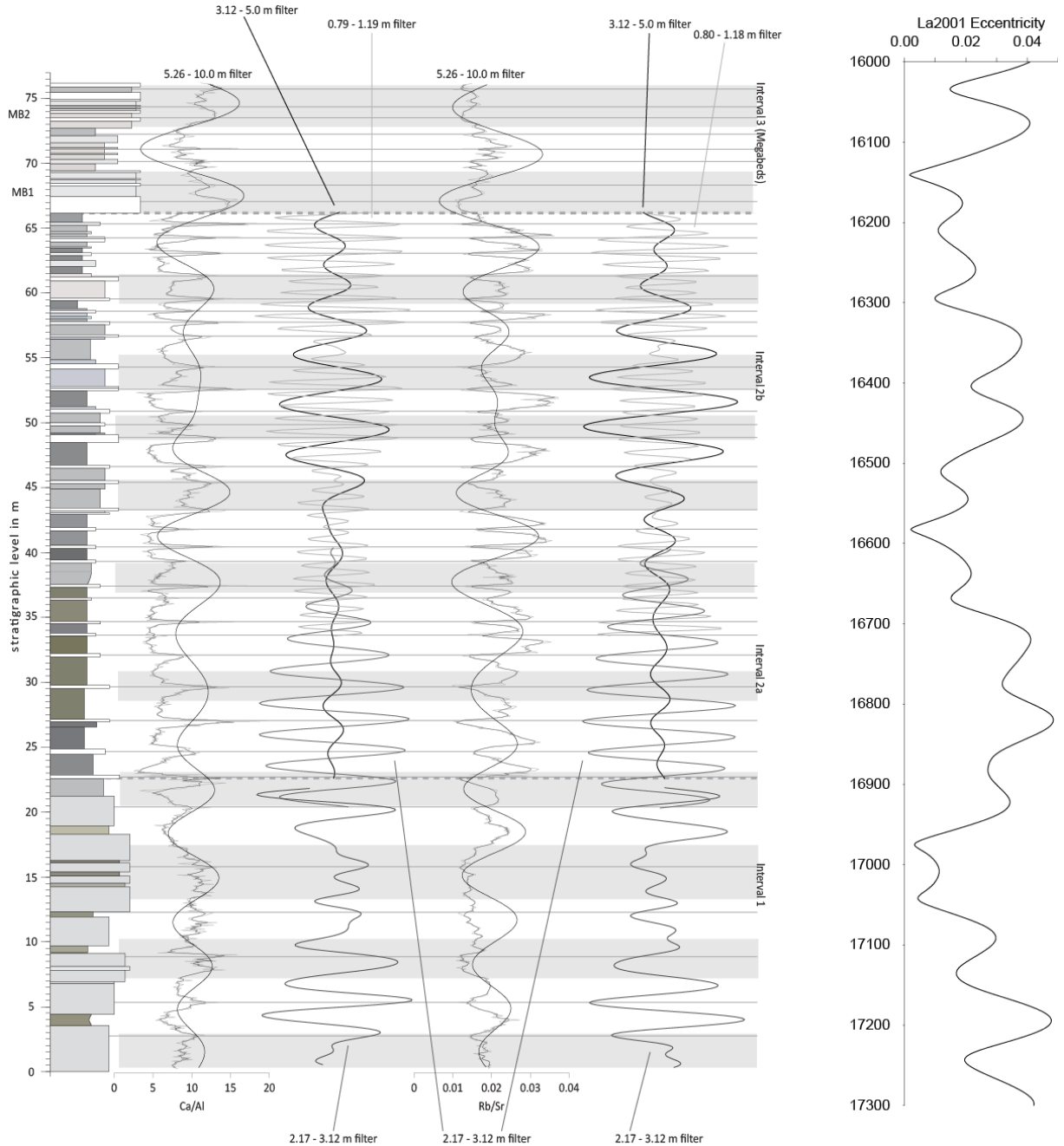


Figure 7: The stratigraphic log is plotted with the Ca/Al and Rb/Sr ratio, with the 3-point moving average (black) on top of the original data (grey). Plotted on top of the records is the long period filter (5.26 - 10.0 m) and next to the records are the filters corresponding to the prominent peaks in the power spectra. Grey bars indicate maxima (minima) in the Ca/Al (Rb/Sr) long period filter. The bandwidth of the different filters is indicated. On the right of the figure the La2001 eccentricity curve [Laskar et al., 2001] is plotted.

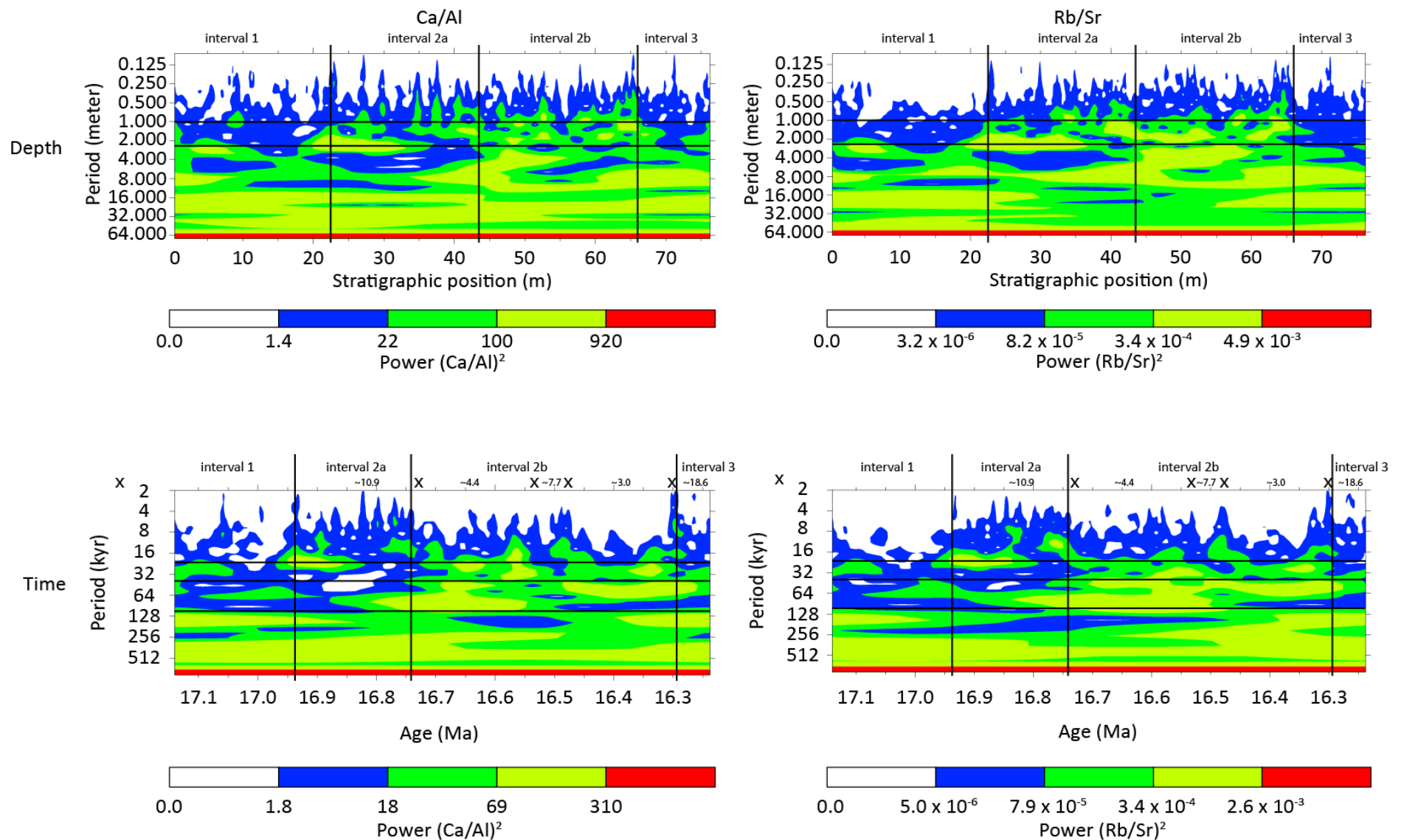


Figure 8: Plots of the wavelet analysis of both Ca/Al (left column) and Rb/Sr (right column) in depth (upper row) and time (lower row) domain. Below all diagrams the scale of the power is indicated: relatively high power in red and relatively low power in white. The intervals are indicated with their corresponding position and ages and dominant periods in depth are indicated with horizontal lines. In the time domain, the horizontal lines at ca. 20 and 40 kyr represent precession and obliquity periods. Just above the diagrams in the time domain, the positions of the GTS2012 [Hilgen *et al.*, 2012] are indicated, with the corresponding sedimentation rate. The left cross is the reversal found in the downward extension [E. Kuikman and S.K. Hüsing, *pers. comm.*].

Table 2: Stratigraphic tie points of the reversals with ages according to GTS2012 [Hilgen *et al.*, 2012]. Reversal C5Dn (y) is based on results of the downward extension [E. Kuikman and S.K. Hüsing, pers. comm.]

Subchron	Position (m)	Age (ka) GTS2012 Hilgen <i>et al.</i> , 2012]
C5Cn.1n (o)	70.62±0.25	16268
C5Cn.2n (y)	64.09±0.69	16303
C5Cn.2n (o)	59.04±1.23	16472
C5Cn.3n (y)	53.57±1.38	16543
C5Cn.3n (o)	45.78±0.94	16721
C5Dn (y)*	-10	17235

7.2 Statistics in time domain

By transferring the Ca/Al and Rb/Sr records from the depth into the time domain, the records are stretched and compressed between the tie points of reversal boundary ages (see table 2; GTS2012 reversal ages + positions) from GTS2012 [Hilgen *et al.*, 2012]. The top of C5Dn is not sampled in this research; its position is based on the downward extension [E. Kuikman and S.K. Hüsing, pers. comm.] and is included as tie point to prevent a misfit in the extrapolation of the lower half of the MCSS composite.

7.2a Spectral analysis

The power spectra of both Ca/Al and Rb/Sr in the time domain are again generated for the entire section and for all intervals, since the basic pattern changes in the different intervals (see Figure 9). The power spectra of interval 3 (Megabeds) in time are similar to those in depth, since there is no significant peak for relatively long periods in most of the Ca/Al and Rb/Sr spectra, only with a short period of *ca.* 2.5 kyr. The “flattening” in the depth spectrum at a period of *ca.* 1.8 m corresponds to a period of *ca.* 9.7 kyr.

In interval 1 there are two similar significant peaks in both Ca/Al and Rb/Sr spectra at *ca.* 28-29 and 10.5 kyr. The filter based on the *ca.* 28-29 kyr period (see Figure 10) matches both the Ca/Al and Rb/Sr record in interval 1, except for the interval between *ca.* 17.05 and 17.0 Ma, equal to the mismatching *ca.* 10-17 m interval in the depth domain.

The power spectra of both Ca/Al and Rb/Sr of interval 2 are dominated by peaks at *ca.* 84 kyr (83.1 for Ca/Al and 85.8 kyr for Rb/Sr), *ca.* 52 kyr (respectively 52.6 and 51.5 kyr), *ca.* 29 kyr (28.9 and 29.9 kyr respectively) and *ca.* 22.5 kyr (22.6 and 22.2 kyr respectively). High frequency peaks are present in the Ca/Al power spectrum at *ca.* 13.9 and 8.9 kyr and in the Rb/Sr spectrum at *ca.* 5.9 kyr. The applied filters of individual intervals (Figure 10) might reveal the origin of periods in the power spectrum.

The two dark marls “e” and “f” at the base of interval 2b are best represented by a long period (*ca.* 80 kyr) filter and the marl-limestone alternation around these marls is best approximated by the 26 to 36 kyr filter. This filter is also a moderate approximation of the variations in “d”, but the marl-limestone alternation around “c” is best approximated by a higher frequency filter (*ca.* 17 – 26 kyr) and UDL and marl “b” fit best with the 36 – 63 kyr filter.

In the depth domain the dark marls could be represented by a *ca.* 4 m filter, but in the time domain there is not one filter available which represents all marls. Furthermore, the marl-limestone alternations around the dark marls “b” and “a” was moderately regular in the depth domain and this cannot be represented by one filter in the time domain. This change is caused by the varying sedimentation rate, which has its origin in the reversal ages from GTS2012 [Hilgen *et al.*, 2012] and therefore it might be possible that one cycle is now represented by two different durations.

7.2b Wavelet analysis

Wavelet analysis is used to confirm the dominant periods in time of the marl-limestone alternation (Figure 8). In the wavelet analyses of both Ca/Al and Rb/Sr interval 1 is not characterised by any very dominant periods, only at the transition to interval 2a the *ca.* 20 kyr period is present. This period disappears at *ca.* 16.82 Ma and shorter periods (*ca.* 13 and 7 kyr) are present. This switch might also be visible in the longer periods in both wavelets, where the dominant period of *ca.* 150 kyr disappears and a *ca.* 70 kyr period is present.

This ca. 70 kyr period is dominant up to the middle of interval 2b (ca. 16.55 Ma in the Ca/Al wavelet; ca. 16.5 Ma in Rb/Sr). In this interval also shorter periods are present (of ca. 45 kyr in both wavelets; ca. 25 kyr in Ca/Al), but also these shorter periods become less prominent at ca. 16.5 Ma. In the C5Cn.2r subchron (ca. 16.54 – 16.47 Ma [Hilgen et al., 2012]) there is only a period of ca. 50 kyr present in the Rb/Sr wavelet. The top of interval 2b of both wavelets is characterised by a dominant ca. 60 kyr period and at ca. 16.35 Ma a period of ca. 30 kyr is present. At the transition from interval 2b to interval 3 dominant periods of ca. 7 and 16 kyr are present in the Ca/Al wavelet. All the longer periods are not significant, because interval 3 is only ca. 50 kyr long and therefore all periods \geq 50 kyr cannot be used.

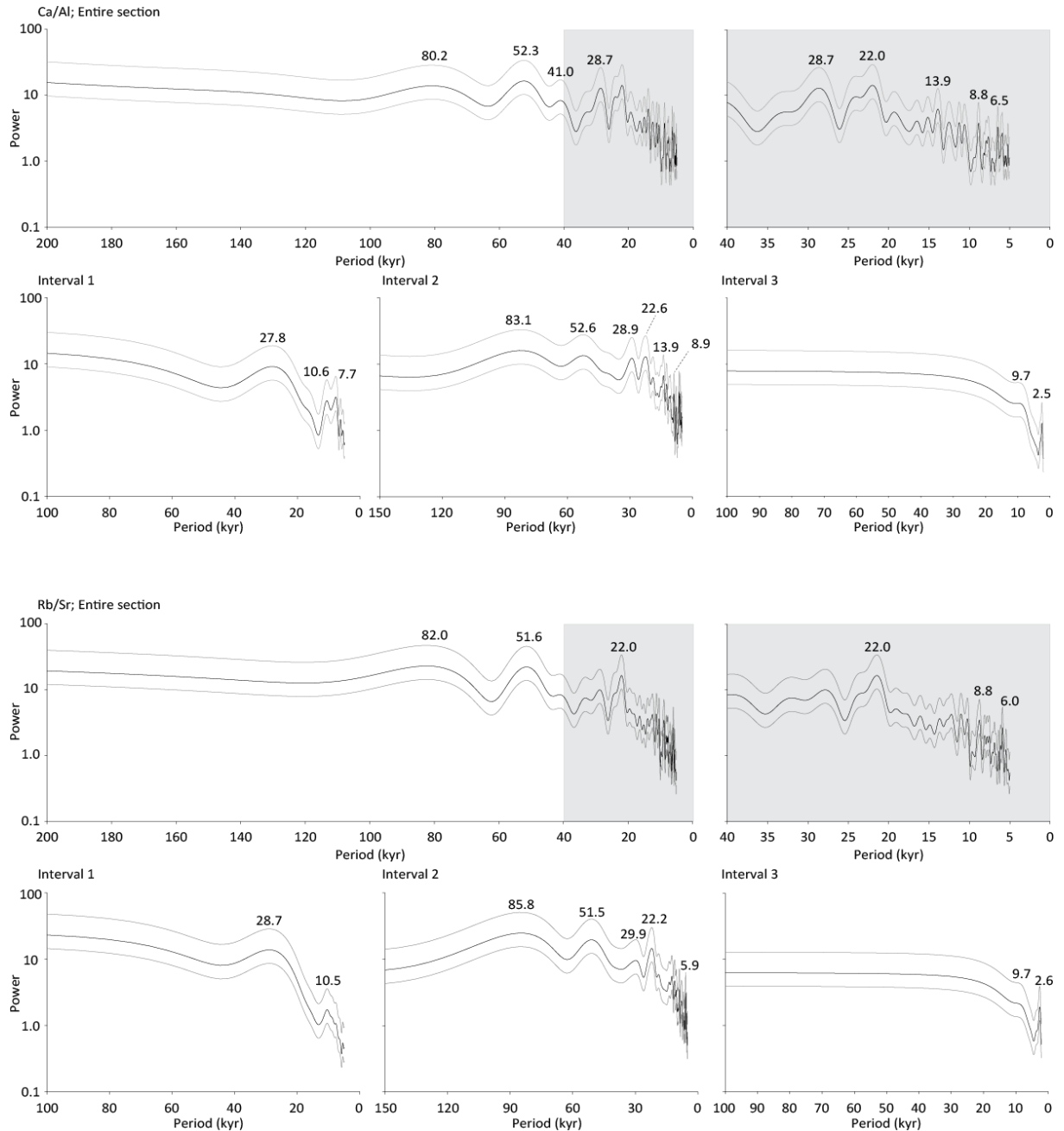


Figure 9: For both the Ca/Al (upper diagrams) and Rb/Sr (lower diagrams) ratios four power spectra are generated (black line) with their 80% confidence (grey lines). The upper two diagrams of both ratios are spectra of the entire section and the grey shaded diagram on the right is an enlargement of the left spectrum. The lower three diagrams are power spectra of single intervals. For all power spectra the period (in kyr) of the peaks are indicated.

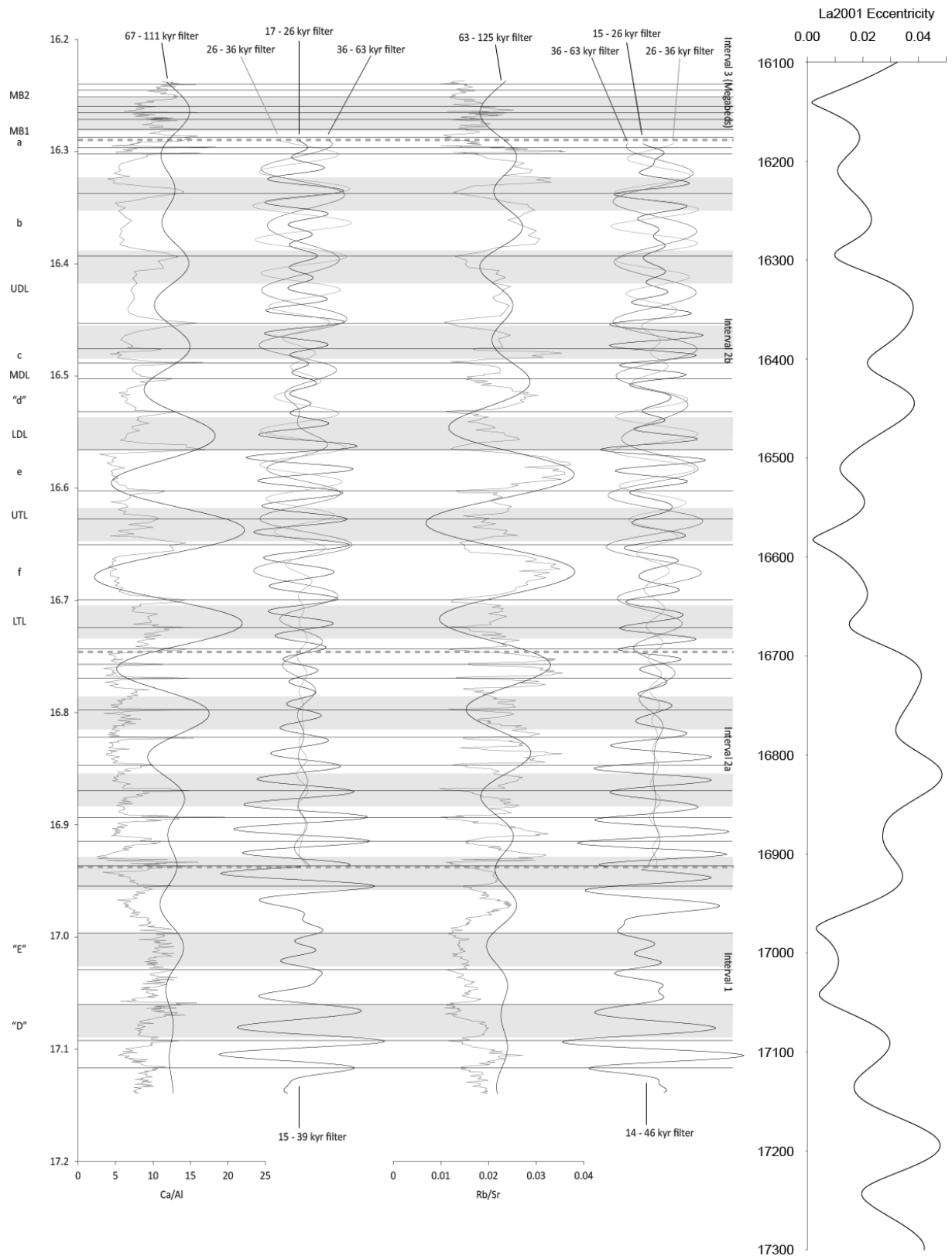


Figure 10: The Ca/Al and Rb/Sr ratio are plotted in time, with the 3-point moving average (black) on top of the original data (grey). Plotted on top of the records is the long period filter (*ca.* 80 kyr) and next to the records are the filters corresponding to the prominent peaks in the power spectra. Grey bars indicate maxima (minima) in the Ca/Al (Rb/Sr) long period filter. The bandwidth of the filters is indicated. On the right of the figure the La2001 eccentricity curve [Laskar *et al.*, 2001] is plotted.

8. Cycle build-up and phase relation

8.1 Cycle build-up

Now that it has been shown that the origin of the cycles present in the section is orbital forcing, one needs to understand the build-up of the basic cycle, which is precession-forced, in order to discuss the phase relation with the orbital parameters. This is an essential step in establishing an astronomical tuning for the MCSS composite section and therefore two short, representative intervals (see Figure 11) are selected and discussed in detail and the repetitive pattern of marl-limestone has been numbered.

An interval of *ca.* 5 m thickness has been chosen from the uppermost part of interval 2b, which will be referred to as cycle interval A) in Figure 11. This interval is characterized by a thinly bedded alternation between marls and limestones (*ca.* 0.5 m), whereby the limestones themselves show an alternation of prominent whitish (greenish-greyish when wet) and less prominent greyish limestones. This pattern is also represented in the CaCO_3 record, where largest maxima in CaCO_3 content are within these prominent whitish limestones and very small increases (relative to the marly intervals) are present in the less prominent greyish limestones. The prominent whitish limestones are further characterized by maxima in Ba/Al and Mn/Al and minima in Rb/Sr , Ti/Al , Si/Al , Zr/Al and specific magnetic susceptibility. Si/Al is furthermore characterized by a rapid increase in the marl in cycle A3 and after a rapid decrease in the limestone at the top of A3 the higher ratio is again present.

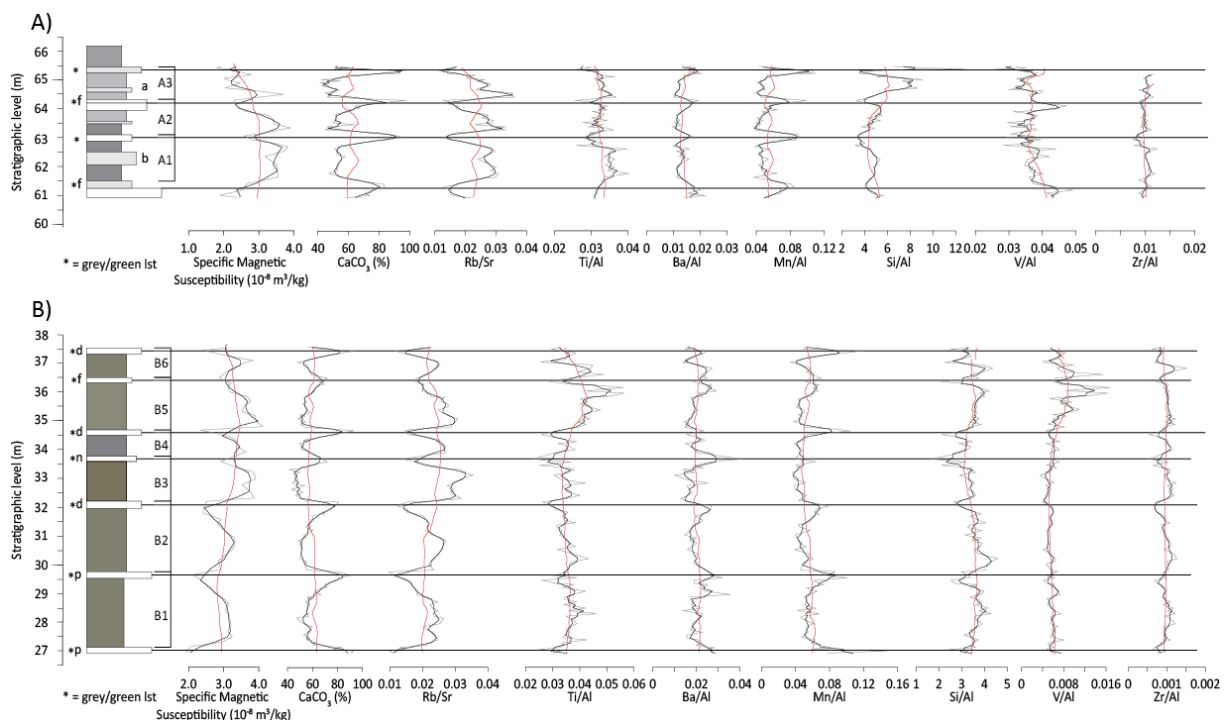


Figure 11: Two short, representative intervals (subinterval A is stratigraphically from *ca.* 61 to 65 m; subinterval B from *ca.* 27 to 38 m) are presented with the lithological log and proxies specific magnetic susceptibility, CaCO_3 content, Rb/Sr , Ti/Al , Ba/Al , Mn/Al , Si/Al , V/Al and Zr/Al . The 3-point (black) and 25-point (red) moving average are plotted on top of the original (grey) data. Asterisks indicate the greenish-greyish limestones with the prominence of the limestones (f=faint; n=normal; d=distinct; p=prominent). In subinterval A the dark marls "a" and "b" are indicated. The successive cycles are indicated per subinterval. See text for discussion.

The phase relation between V/Al and CaCO_3 content is not as straightforward as for the other elements. There seems to be a small increase in V/Al in the lower part of the maxima in CaCO_3 in the upper two basic cycles (cycle A2 and A3), whereas in the lower basic cycle A1 the increase seem to occur below the CaCO_3 maximum, within the grey marl and less prominent greyish limestone, thus preceding the prominent whitish limestone formation.

The second interval, referred to as cycle interval B in Figure 11, is *ca.* 11 m long and is characterized by an alternation of thick soft dark brown marls and thin prominent to faint whitish limestones (greenish-greyish when wet). The distance between the limestones is *ca.* 2.5 m for the lower three limestones (cycle B1 and B2) and changes to a pattern of 2m-1m-2m-1m for the upper four limestones in cycle B3 to B6. The phase relation between the white limestones and the elements is similar as in interval A, with maxima in Ba/Al and Mn/Al and minima in Rb/Sr, Ti/Al, Si/Al and Zr/Al coinciding with the maxima in CaCO_3 content (note the differences in scale for the elements). V/Al is again not as straightforward as the other elements and seems to be correlated to the Ti/Al record in cycle B5 and B6, especially at *ca.* 36 m at the top of the marl. On the other hand, it is located right at the base of the CaCO_3 maxima in cycle B2, B3 and B6, which is similar to cycle interval A2 and A3. In cycle B1 and B4 small amplitude minima in V/Al coincide with the maxima in CaCO_3 .

The main advantage of combining several proxies with a different normalizing element (such as Ti/Al and Rb/Sr) is the different response of each element to e.g. diagenesis and (astronomically forced) climate changes. In most cases normalization to Al excludes diagenetic effects, but it cannot be ruled out that some oxides from the seawater remove some Al from the sediment [Kryc *et al.*, 2003]. Furthermore, the use of one common divisor (often done with Al) can lead to false correlations, as the provenance of the detrital input can change because of climate changes [e.g. Krom *et al.*, 1999].

8.2 Phase relation with insolation and precession

It is important to understand whether the limestones in the astronomically forced marl-limestone alternation are related to boreal precession minima/summer insolation maxima. Both phase relations are reported in the Mediterranean region, e.g. limestones on Sicily are correlated to insolation minima (boreal precession maxima) [Hilgen, 1991], but the limestones of La Vedova correlate to insolation maxima (boreal precession minima) [Hüsing *et al.*, 2010; Mourik *et al.*, 2010]. Maxima of Ti/Al and Zr/Al in the marls are an indication that the Mediterranean region was dry and arid with elevated aeolian input [Wehausen and Brumsack, 2000], which is related to precession maxima/insolation minima [Foucault and Mélières, 2000; Lourens *et al.*, 2001]. This is supported by maxima in Rb/Sr, since Sr can easily substitute for Ca in Ca-rich minerals (carbonates) and Rb is closely related to K in mineral formation [Heier and Billings, 1970] and by maxima in specific magnetic susceptibility, caused by higher terrestrial input [Ellwood *et al.*, 2000]; this is similar to the younger La Vedova section [Hüsing *et al.*, 2010; Mourik *et al.*, 2010].

The maxima in Ba/Al ratio (coinciding with maxima in CaCO_3) are caused by higher productivity [van Santvoort *et al.*, 1996; Weldeab *et al.*, 2003]. This is in agreement with the Mn/Al record, which indicates well oxygenated waters during the deposition of the limestones [Calvert and Pedersen, 1993]. V/Al peaking just below a limestone bed is an indication of reducing conditions, as can be observed in sapropelitic layers in the younger part of the La Vedova section at *ca.* 13.6 Ma [Mourik *et al.*, 2010]. On the other hand, it is also possible that V/Al is absorbed into Mn oxyhydroxides and will therefore coincide with the CaCO_3 maxima [Hastings *et al.*, 1996; Morford and Emerson, 1999].

Si/Al is influenced by biogenic silica, (free) quartz and silicate minerals and is thus hard to use as a proxy of insolation. However, in these records it peaks in the marls and these variations are thus probably caused by terrestrial input.

Overall, the here described elemental pattern and the correlation to insolation, along with a marl-(faint) limestone-marl-(prominent) limestone alternation, seems comparable to the quadruplet records of the younger part of La Vedova [Mourik *et al.*, 2010].

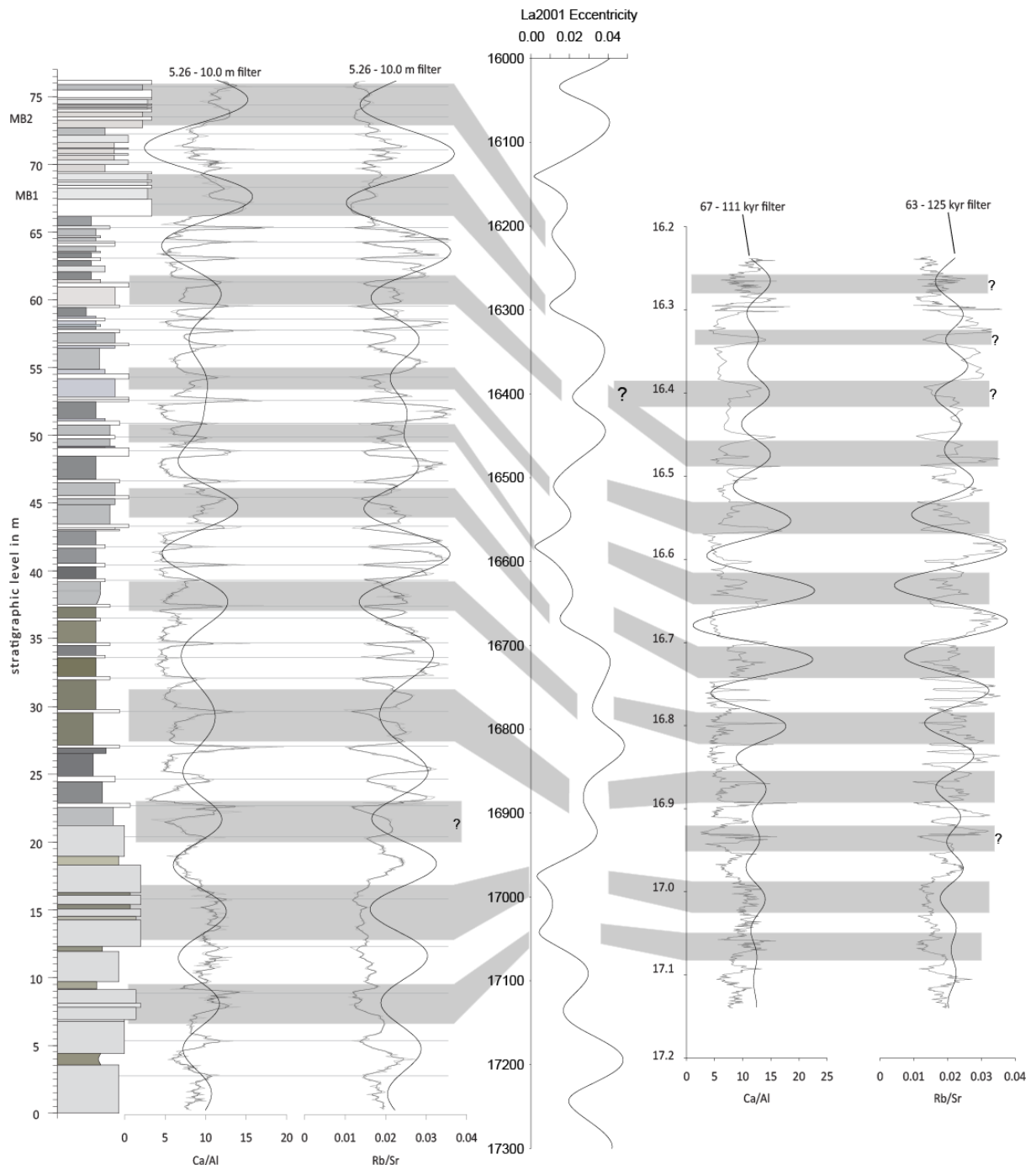


Figure 12: Stratigraphic log plotted with corresponding changes in Ca/Al and Rb/Sr, where the 3-point moving average (black) is plotted on top of the original data (grey). Maxima (minima) in long period filters (*ca.* 7.6 m; 80 kyr) of Ca/Al (Rb/Sr) in both depth and time domain are correlated to the minima in La2001 eccentricity curve and show mismatches. In the depth domain at *ca.* 22 m, as well as in the time domain at *ca.* 16.95 Ma, there seems to be an additional cycle present. In the top of the time domain the top of the record is poorly constrained. See text for discussion.

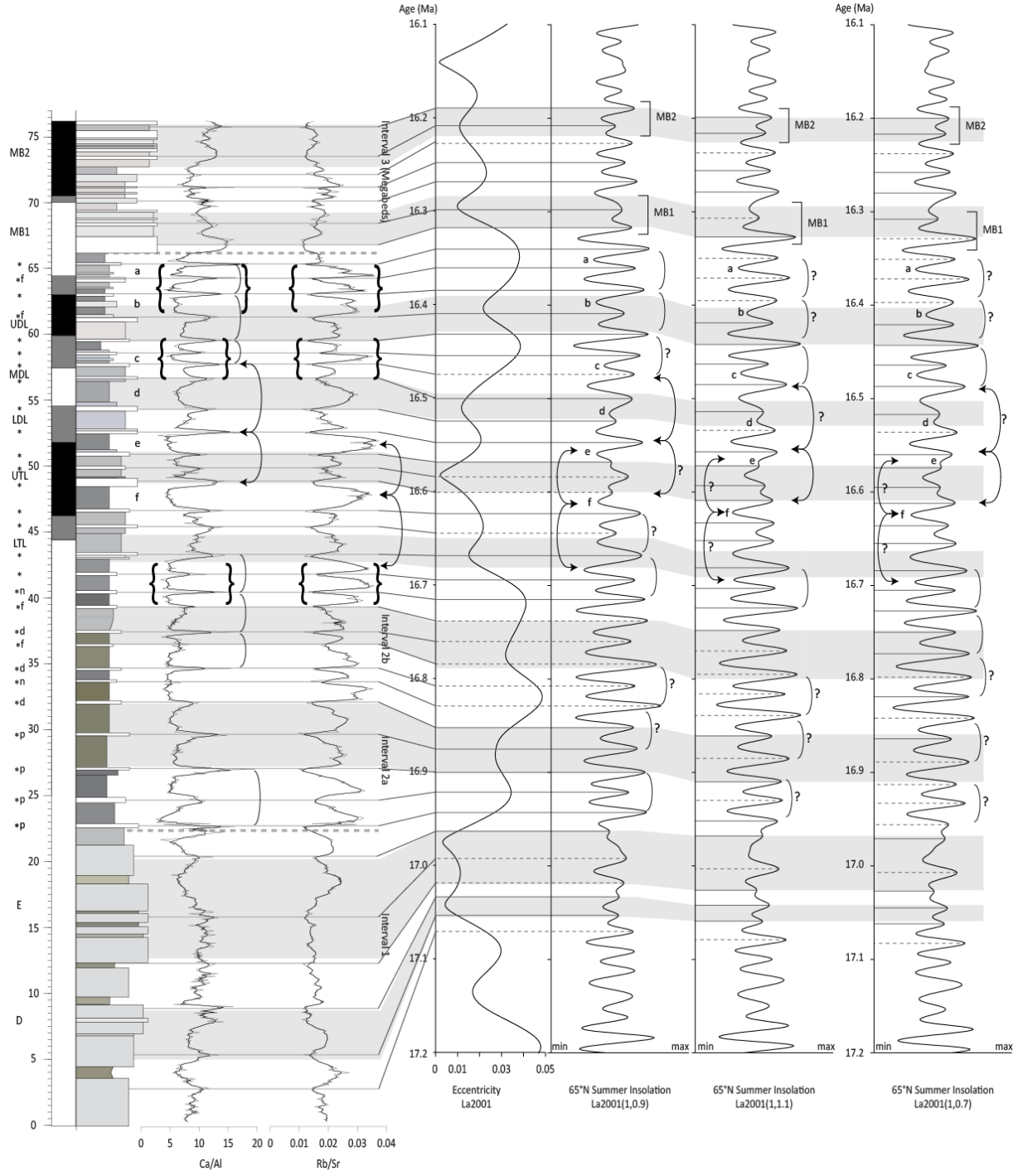


Figure 13: The stratigraphic log is plotted on the left side of the figure, with the names of the prominent beds "D" and "E" in interval 1; LTL, UTL, (Lower and Upper Triple Limestone), LDL, MDL and UTL (Lower, Middle and Upper Double Limestone) and the prominent dark marls "a" to "f" in interval 2; MB I and II (Megabed I and II) in interval. Next to the stratigraphic log is the magnetostratigraphy indicated, where the normal (black) and reverse (white) polarities are plotted with the uncertainties around reversals (grey). On the right side of the stratigraphic log the 3-point moving average (black) of Ca/Al and Rb/Sr are plotted on top of the original data (grey) and the intervals. Brackets indicate the precession-obliquity interference pattern, brackets with arrows indicate the switch in the precession-obliquity interference pattern. Braces denote bundling. On the right side of the figure the La2001 eccentricity curve and three 65°N summer insolation curves (respectively La2001_{1,0.9}; La2001_{1,1.1}; La2001_{1,0.7}) are presented. Correlations between the record and proxies and the eccentricity curve are indicated by grey bars. Correlations on precession scale between the proxies are indicated by lines, where a continuous (dotted) line denotes a good (poor) match. Question marks next to interference patterns in the solutions indicated a non-observed or non-matching interference pattern.

9. Astronomical tuning

9.1 Astronomical tuning

Using the correlation to the La Vedova section [Hüsing *et al.*, 2010; Mourik *et al.*, 2010; Turco *et al.*, 2011] the age of the upper part of MCSS is constrained to the late Burdigalian. Using the here presented magnetostratigraphy, the top of the MCSS composite section is dated around 16.2 Ma and this is the starting point of the astronomical tuning. The first step in an astronomical tuning is the recognition of the 405 kyr eccentricity cycle, which modulates the *ca.* 100 kyr eccentricity cycles. In the Late Burdigalian successive 405 kyr minima are present at *ca.* 16.2, 16.6 and 17.0 Ma [Laskar, 2001] and therefore low amplitude variations in eccentricity and precession, since eccentricity modulates precession.

Low amplitude changes in the proxies are present in the top and base of MCSS (interval 1 and 3) (see Figure 13) and these intervals should therefore be correlated to long-term eccentricity minima. The middle interval 2 is characterized by high amplitude variations in the elements and prominent dark marls, which is correlated to long- and short-term eccentricity maxima and therefore maximum amplitudes in precession.

Below Megabed I the dominant marl-limestone alternation and the Ca/Al and Rb/Sr records show two bundles of both Ca/Al and Rb/Sr at *ca.* 58 and 65 m (indicated in Figure 13 as braces). This bundling is very characteristic for *ca.* 100 kyr eccentricity maxima and these bundles together are indicative of a 405 kyr eccentricity maximum. Normally, three or four *ca.* 100 kyr eccentricity cycles are present in the maximum of one 405 kyr cycle during late Burdigalian times, but the 405 kyr eccentricity maximum at *ca.* 16.4 Ma is strongly influenced by the 2.4 Myr eccentricity minimum [Laskar, 2001], giving rise to only two pronounced 100 kyr eccentricity maxima. This pattern fits very well with the bundling described at *ca.* 58 and 65 m.

At *ca.* 41 m bundling is again visible (braces in Figure 13), especially in Rb/Sr between the prominent light grey marl at *ca.* 39 m and LTL, and this should be related to the relatively strong *ca.* 100 kyr eccentricity maximum, which is present at *ca.* 16.72 in the eccentricity curve [Laskar, 2001]. Interval 2a (below *ca.* 43 m) shows regular alternations of strong and weak amplitudes, which are characteristic for precession/obliquity interference patterns. In combination with the overall high amplitudes, this interval can only correspond to an interval with strong eccentricity and precession/obliquity interference, which is exactly the pattern in the insolation curves between *ca.* 16.95 and 16.65 Ma. This is the expression of a 405 kyr eccentricity maximum, combined with a *ca.* 2.4 Myr eccentricity minimum.

Subsequently, the entire interval between *ca.* 41 and 58 m is correlated to the two short eccentricity cycles with low precession amplitudes between *ca.* 16.66 and 16.5 Ma. LTL is tuned to the eccentricity minimum at *ca.* 16.66 Ma, UTL to the minimum at *ca.* 16.58 Ma and the interval around "d" to the minimum at *ca.* 16.5 Ma (although poorly constrained). This interpretation is confirmed by spectral analysis and filtering in depth domain (see Figure 13), in which the *ca.* 7.6 m filter corresponds to this correlation.

As mentioned earlier, interval 3 with two Megabeds, is correlated to the 405 kyr eccentricity minimum around *ca.* 16.2 Ma. It seems most likely to correlate the relatively large amplitude variations between these two Megabeds to an eccentricity maximum at *ca.* 16.26 Ma and the Megabeds to eccentricity minima at *ca.* 16.2 and 16.3 Ma.

Similarly, interval 1 (with indurated beds "D" and "E") is characterized by very low amplitude variations and is therefore correlated to the *ca.* 405 kyr eccentricity minima at *ca.* 17.0 Ma. The two indurated beds "D" and "E" are separated by a less prominent, marly interval with relatively low amplitude variations. These indurated beds "D" and "E" are therefore correlated to the two eccentricity minima at *ca.* 17.04 and 16.97 Ma, which are unusually close together as the *ca.* 100 kyr eccentricity maximum is actually only *ca.* 70 kyr long. Furthermore, the amplitude of this short eccentricity maximum is very low and therefore the relatively low variations in the marly interval between "D" and "E" is correlated to this "suppressed" eccentricity maximum at *ca.* 17.0 Ma.

Between the minima at 16.97 Ma (with "E") and 16.77 Ma (with the grey marl) only one *ca.* 100 kyr eccentricity minimum is present. However, the filters in depth and time domain (respectively *ca.* 7.6 m and 80 kyr, see Figure 12) showed the presence of two cycles in this interval. This is considered to be a mathematical misrepresentation, probably caused by a change in sedimentation rate. This hypothesis can be confirmed or rejected by tuning the records to precession.

Another problem in the filtering is present at the top of the MCSS composite. Based on the eccentricity tuning, each Megabed is correlated to one *ca.* 100 kyr eccentricity minimum, but according to the magnetostratigraphical age model the entire interval 3 is only *ca.* 54 kyr long (see Figure 12), constrained by the reversal ages from GTS2012 [Hilgen *et al.*, 2012]. The corresponding high sedimentation rate change from C5Cn.2n (*ca.* 3.0 cm/kyr) to C5Cn.1r (*ca.* 18.6 cm/kyr) was already an indication that these ages are not completely accurate and based on this eccentricity tuning (Figure 13) this reversal will be slightly older (*roughly* 16.36 Ma, compared to 16.303 Ma of GTS2012 [Hilgen *et al.*, 2012]). Furthermore, the reversal between C5Cr and C5Cn.3n will also shift in time, but this reversal becomes much younger (*roughly* 16.64 Ma, relative to the 16.721 Ma of GTS2012 [Hilgen *et al.*, 2012]).

The next step is tuning to precession cycles and this depends on the values for dynamic ellipticity (DE) and tidal dissipation (TD) used in the astronomical solution. In Figure 13 three different La2001 solutions [Laskar, 2001] of 65°N insolation are plotted, since these give the best fit for the Mediterranean environment [Lourens *et al.*, 2001]. The DE is equal to present-day (and thus 1) and the values (0.7, 0.9 and 1.1) for TD vary. Since the values for DE and TD changed over time, changing these values will result in a different interference pattern between obliquity and precession [Pälike and Shackleton, 2000; Hüsing *et al.*, 2007] and thus different ages for the insolation maxima. Tuning of the La Vedova section has shown that the best fit with the intricate pattern of the section was achieved by using the (1,0.9) solution, instead of the (1,1) solution, which is valid for present-day. For the here presented astronomical tuning does not use the (1,1) solution, but the La2001_(1,0.7), La2001_(1,0.9) and La2001_(1,1.1) solutions are plotted as it seems that a combination of several solutions might give a better representation of the Ca/Al record.

In the upper part (*ca.* \geq 51 m; \geq 16.56 Ma) the La2001_(1,0.9) solution gives the best fit with Ca/Al, especially with the interference pattern present around marls "a" to "e" (indicated with brackets in Figure 13). However, between "c" and "d" there is one limestone very prominent with respect to the La2001_(1,0.9) solution. Around "f" the correlation in interference patterns between Ca/Al and the La2001_(1,0.9) solution is very poor and this can be solved by selecting another solution, such as the La2001_(1,0.7) or the La2001_(1,1.1) solutions, which are very similar in this interval.

Both show a good correlation with the Ca/Al record, especially in the interference pattern between UTL and LDL (brackets with arrows in Figure 13). However, these solutions show problems to the eccentricity tuning in the interference pattern around marls "b" and "c", which is correlated to the *ca.* 16.4 Ma eccentricity minimum, but in the La2001_(1,0.7) and La2001_(1,1.1) solutions this interval is almost coinciding with the *ca.* 16.44 Ma maximum.

The prominent marls "a" to "f" might now be related to the variations in obliquity, since there is a marl present in between the marls "a" to "f". Between "c" and "d" and between "e" and "f" two less prominent marls are present, and this switch is characteristic for precession-obliquity interference (brackets with arrows in Figure 13). This switch is also present in the limestones around "d", where the interference pattern two low amplitude maxima, surrounded by two large amplitude maxima (brackets with arrows in Figure 13).

In interval 2a the relative prominence of the greenish-greyish limestones is indicated, which is very similar to the relative changes in Ca/Al. The Ca/Al and the prominence of the limestones are characterized by a very specific interference pattern, but this complete pattern is not present in any of the solution. In the upper and lower part of interval 2a the interference pattern of La2001_(1,0.9) matches the Ca/Al ratio best, but in the middle part the interference pattern does not match. Over the entire interval 2a the La2001_(1,0.9) solution seems to represent the Ca/Al record best.

The tuning in interval 1 is difficult because of the small amplitude changes and therefore all three presented solutions match to some extent, except for the strong insolation maximum at *ca.* 17.0 Ma

and ca. 17.08 Ma. As soon as the records of the downward extension [*work in progress, S.K. Hüsing*] can be combined with MCSS composite, the tuning of the lowest interval might become more robust. For the MCSS composite Ca/Al record, the La2001_(1,0.9) solution gives the best fit and this solution will be used to calculate astronomical ages for the reversal boundaries.

A very short lag between monsoon and insolation might be applicable for these records [Weber and Tuenter, 2011], but this lag is not defined for late Burdigalian times and therefore no lag is used in the correlation between insolation maxima from the La2001_(1,0.9) solution and the greenish-greyish limestones. Using La2001_(1,0.9) insolation ages, the MCSS composite section is constrained between 17.087 and 16.183 Ma (see appendix 1 for the tie points used in the tuning). Megabed I is present between 16.324 and 16.279 Ma (duration: 45 kyr) and Megabed II between 16.218 and 16.183 Ma (35 kyr).

9.2 Consequences tuning

This tuning has consequences for change in the isotope records (see Figure 14), which are now constrained in time and not only in depth. The gradual decreases in $\delta^{13}\text{C}$ and $\delta^{18}\text{O}$ (as it was described in the depth domain) are actually quite rapid at ca. 16.98 Ma, whereas the rapid increase in $\delta^{13}\text{C}$ remains rapid and occurs at ca. 16.65 Ma. The three maxima in $\delta^{18}\text{O}$ around ca. 17.0 Ma are ca. 40 kyr spaced apart and therefore likely to be forced by obliquity. This might also be visible around 16.5 Ma, but the sampling resolution is too low to correlate these peaks to obliquity forcing.

The changing sedimentation rate hypothesis is also confirmed by the here presented tuning. In the magnetostratigraphic age model a change in sedimentation rate was required to match the polarity pattern to the GTS2012 [Hilgen et al., 2012] (somewhere in C5Cr) and this tuning places a gradually changing sedimentation rate at ca. 32 to 40 m, which corresponds to ca. 16.85 to 16.75 Ma. This is also observed in the stratigraphic log and proxy records, because the dominant ca. 2-2.5 m period in the lower half of interval 2a is gradually changing to a ca. 1 m period in the uppermost part.

This astronomical tuning is dominated by precession and the phase relation between the marl-limestone alternation is similar to the phase relation at La Vedova [Hüsing et al., 2010; Mourik et al., 2010]. This implies that the climatic system, dominated by precession and responsible for the sapropel formation, is already present during late Burdigalian times.

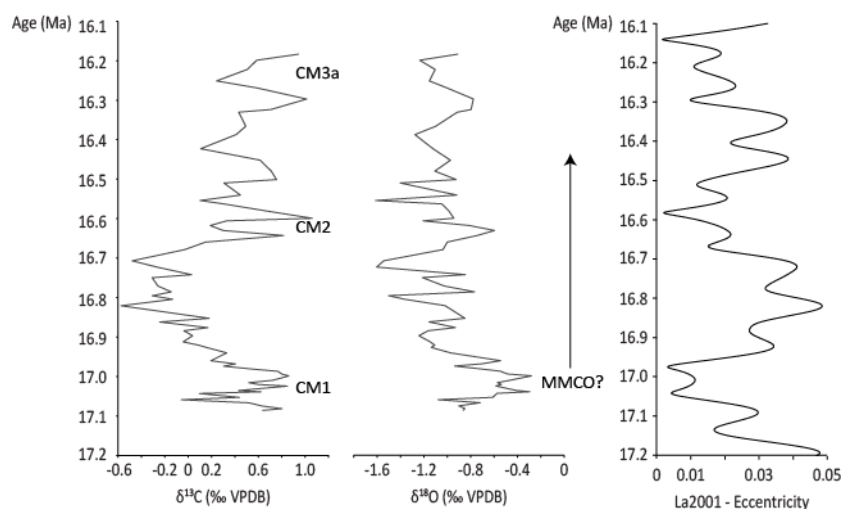


Figure 14: $\delta^{13}\text{C}$ (left diagram) and $\delta^{18}\text{O}$ (middle diagram) ratios (in ‰) plotted in time with on the right the La2001 eccentricity curve. CM1-CM3a are recognized in the $\delta^{13}\text{C}$ and the onset of the MMCO in the $\delta^{18}\text{O}$.

10. Discussion

10.1 Tuning

10.1a Comparison with GTS2012 and Billups04

The ages of the reversals according to the GTS2012 [Hilgen *et al.*, 2012] and this tuning differ significantly at the reversal C5Cn.2n (y) (61 ± 14 kyr older) and at reversal C5Cn.3n (o) (86 ± 14 kyr younger) (see table 3). Reversal C5Cn.1n (o) is *ca.* 100 kyr younger in the Billups04 age model relative to the here presented tuning and this difference slowly increases to *ca.* 140 kyr to the reversal C5Cn.3n (o).

Compared to the differences in reversal ages (from $+61\pm14$ to -86 ± 14 kyr) between GTS2012 and the astronomical tuning, the Billups04 tuning is more consistent with this tuning, but consistently *ca.* 100 kyr younger. If the eccentricity tuning of this research is shifted *ca.* 100 kyr upwards (younger) to get a similar age as the Billups04 reversal ages, the very characteristic pattern of the *ca.* 100 kyr eccentricity cycles in MCSS does not match anymore. The *ca.* 100 kyr offset is probably related to a major hiatus in the top of their record (ODP core 1090), which causes a misfit in their eccentricity filters (see Figure 3c in Billups *et al.*, 2004). The best example is the well-expressed 405 kyr eccentricity maximum at *ca.* 16.8 Ma, where three *ca.* 100 kyr eccentricity maxima are visible. In the filters applied by Billups *et al.* (2004) only two cycles are present in the filter, which is a clear indication that the tuning is not correct in that interval.

The Early Miocene reversal ages (including C5Cn) from GTS2012 (and corresponding durations of the subchrons) are originally published ATNTS04 [Lourens *et al.*, 2004] and are based on an interpolation of the spreading rate of the Antarctic-Australian plate pair, but only two tie points were used for the Early Miocene (at 16.0 and 23.0 Ma [Lourens *et al.*, 2004]). For the early Middle Miocene and late Early Miocene a spreading rate of *ca.* 67.7 mm/yr was used, but this required a “minor rate change” at reversal C5En (o) (at *ca.* 18.52 Ma) to fit the 23.0 tie point. This caused probably the large offset in the reversal ages of C5Cn.3n (o).

Table 3a (upper): Revised reversal ages, relative to earlier published reversal ages GTS2012 [Hilgen *et al.*, 2012] and Billups04 [Billups *et al.*, 2004]. Uncertainties in tuned ages originate from uncertain positions of reversal boundaries.

Table 3b (lower): Durations of subchrons in comparison with earlier published durations as GTS2012 [Hilgen *et al.*, 2012] and Billups04 [Billups *et al.*, 2004]. Uncertainties in durations originate from uncertain positions of reversal boundaries.

Reversal	Position (m)	Age (ka) GTS2012 [Hilgen <i>et al.</i> , 2012]	Age (ka) Billups04 [Billups <i>et al.</i> , 2004]	Tuned Age (ka)	Δ to GTS2012 (ka)	Δ to Billups04 (ka)
C5Cn.1n (o)	70.62 ± 0.25	16268	16161	16257 ± 6	-11 ± 6	96 ± 6
C5Cn.2n (y)	64.09 ± 0.69	16303	16255	16364 ± 14	$+61\pm14$	109 ± 14
C5Cn.2n (o)	59.04 ± 1.23	16472	16318	16446 ± 26	-26 ± 26	128 ± 26
C5Cn.3n (y)	53.57 ± 1.38	16543	16405	16533 ± 17	-10 ± 17	128 ± 17
C5Cn.3n (o)	45.78 ± 0.94	16721	16498	16635 ± 14	-86 ± 14	137 ± 14

Subchron	Duration (kyr) GTS2012 Hilgen <i>et al.</i> , 2012]	Duration (kyr) Billups04 [Billups <i>et al.</i> , 2004]	Tuned Duration (kyr)	Δ to GTS2012 (kyr)	Δ to Billups04 (kyr)
C5Cn.1r	35	94	107 ± 20	$+72\pm20$	$+13\pm20$
C5Cn.2n	169	63	82 ± 40	-87 ± 40	$+19\pm40$
C5Cn.2r	71	87	87 ± 43	$+16\pm43$	0 ± 43
C5Cn.3n	178	93	102 ± 31	-76 ± 31	$+9\pm31$

A significant difference is also present in the duration of subchron C5Cn.1r (35 kyr; 16.303-16.268 Ma, GTS2012 [Hilgen *et al.*, 2012]) and duration based on the here presented tuning (107 kyr; 16.364-16.257 Ma). The duration of the here presented tuning is confirmed by the independently tuned duration of 94 kyr for C5Cn.1r (16.255-16.161 Ma; Billups04 [Billups *et al.*, 2004]), although the exact age is off by *ca.* 100 kyr. The short duration for C5Cn.1r occurs already in early published time scales [e.g. Heirtzler *et al.*, 1968; Blakely, 1974].

Additional independent age control of the Columbia River Basalt Group [Jarboe *et al.*, 2010] suggest that both the GTS2012 [Hilgen *et al.*, 2012] and Billups04 [Billups *et al.*, 2004] are not completely correct. The authors have problems relating their findings to either of these timescales, since the GTS2012 age model results in very large changes in eruption rates (19 times larger in C5Cn.1r than C5Cn.3n). On the other hand, the $^{40}\text{Ar}/^{39}\text{Ar}$ age of the “Steens Reversal” (C5Cr-C5Cn.3n) is at 16.73 +0.13/-0.08 Ma [Jarboe *et al.*, 2010], which is inconsistent with the Billups04 age (16.498 Ma). The age of the Steens Reversal is not significantly different from the here presented astronomically tuned age and the result of the here presented tuning is a more constant eruption rate in the Columbia River Basalt Group.

10.1b Uncertainties tuning

The main problems in the tuning occur in the minima of 405 kyr eccentricity cycles, where the interference pattern of the solutions does not always match the (observed) interference pattern of the proxies. The most striking example is the 405 kyr eccentricity minimum at *ca.* 16.6 Ma, which can either fit on the eccentricity-scale by a mismatch in the precession-obliquity interference pattern (the La2001_(1,0.9) solution in Figure 13) or by a good fit in the interference pattern, but a mismatch in the eccentricity minimum at *ca.* 16.4 Ma (the La2001_(1,0.7) and La2001_(1,1.1) solution in Figure 13).

In the 405 kyr eccentricity minimum of interval 1 (at *ca.* 17.0 Ma) the tuning is again not perfect. In all La2001 solutions there is an unusually thick precession cycle present (at *ca.* 16.98 Ma), which is now tuned to the thicker interval between *ca.* 16 and 20 m. When this thicker precession cycle is tuned to another (thinner) interval, the sedimentation rate will change significantly over a short period of time, which seems unlikely.

On the other hand, the tuning of this thicker precession cycle to the thicker depth interval causes a mismatch with the *ca.* 100 kyr eccentricity maximum at *ca.* 17.0 Ma (although it is only *ca.* 70 kyr long), which is expected in the more marly interval between “D” and “E”. However, based on the correlation of this thick precession cycle to the thicker interval between *ca.* 16 and 20 m, the eccentricity maximum is present in “E”. On the other hand, the expected larger amplitude precession cycle (depending on the solution it is either a larger maximum or minimum) is not well expressed in the data of the marly interval between “D” and “E”.

These uncertainties in the tuning are caused by differences in the La2001 solutions, but in theory there should be a solution with a good match with the data. However, many La2001 solutions (in which DE is kept constant at 1 and TD varies 0.1 and 1.2, in step sizes of 0.1) cannot reproduce the interference pattern in Ca/Al and Rb/Sr and therefore it might be possible that there is a small error in the solution. On the other hand, it might also be possible that using a smaller step size for TD in a La2001 solution might be enough to solve the mismatch in the interference pattern. More research is definitely required to solve this discrepancy.

Next to the uncertainties in the tuning, the reversal boundaries are not always well-defined in this record. The base of subchron C5Cn.1r is constrained on one sample and since there is a possibility that this sample is not actually reversed, but by accident showing a reversed polarity (the quality of the data is after all not excellent). Therefore the uncertainty the reversals might increase. However, even if the uncertainty of the reversal is expanded and consequently C5Cn.1r is only present from *ca.* 66.80 m upwards, the tuned age of the reversal is still older (*ca.* 16.32 Ma) from the GTS2012 age of 16.303 Ma [Hilgen *et al.*, 2012].

10.2 Isotopes

The large-scale changes in the isotope records of MCSS can be compared to the worldwide recognized oxygen isotope ("Mi"-events) excursions [Miller *et al.*, 1991; Scott *et al.*, 1995; Miller and Mountain, 1996] and carbon isotope ("CM"-events) excursions [Woodruff and Savin, 1991; Holbourn *et al.*, 2007]. Using the here presented tuning, the isotope records of depth are transferred into time. The maxima in $\delta^{13}\text{C}$ are present in long-term eccentricity minima, based on the here presented astronomical tuning.

This is similar to ODP site 1237, where the nomenclature of the CM-events is revised (CM3 to CM5 all consist of two 405 kyr cycles) [Holbourn *et al.*, 2007]. The maximum in $\delta^{13}\text{C}$ at *ca.* 17.0 Ma (see Figure 14) can be correlated to the so-called CM1 and the maximum at *ca.* 16.6 Ma to CM2. The top of the record might be correlated to CM3a, although the amplitude variations are not very large. This is in agreement with the record of ODP site 1237, which show a relatively high amplitude minimum between CM1 and CM2 and a relatively CM2 and CM3a (see Figure 3 of Holbourn *et al.*, 2007).

The $\delta^{18}\text{O}$ record of MCSS peaks at *ca.* 17.0 Ma (see Figure 14), which correlate with the 405 kyr eccentricity minimum at *ca.* 17.0 Ma. The other 405 kyr eccentricity minima at *ca.* 16.6 and 16.2 Ma are not as well expressed in the $\delta^{18}\text{O}$ record, but the small increase in $\delta^{18}\text{O}$ at these positions might be related to these eccentricity minima.

The maximum in $\delta^{18}\text{O}$ can be correlated to the start of the final phase of warming leading up to the Middle Miocene Climatic Optimum (*ca.* 0.5‰ decrease, [Zachos *et al.*, 2001]), but it is also possible that it is related to the Mi1c event. Mi1c is found at DSDP Site 593 in the southwest Pacific [e.g. Scott *et al.*, 1995; Cooke *et al.*, 2008]. On the other hand, this event is not recognized in Atlantic [Billups *et al.*, 2004] or eastern Pacific records [Holbourn *et al.*, 2007]. Therefore it is more likely that this represents the start of the MMCO than the poorly constrained Mi1c event.

The large fluctuations in the $\delta^{13}\text{C}$ record can be explained by changes in the carbon reservoir [Holbourn *et al.*, 2007 and references therein]. The authors suggest that enhanced organic carbon burial during eccentricity minima might reinforce atmospheric CO₂ drawdown and global cooling. On the other hand, during eccentricity maxima net CO₂ is released to the atmosphere and the marine ^{13}C carbon reservoir gets depleted as consequence of a relatively shallower CCD and higher production of carbonates in tropical shallow seas.

The $\delta^{18}\text{O}$ decrease between *ca.* 17.0 and 16.9 Ma might be an indication that the $\delta^{13}\text{C}$ hypothesis is also valid for this record, since $\delta^{18}\text{O}$ is generally related to waxing and waning of ice sheets or regional variations in salinity, depending on the regional water budget [Billups and Schrag, 2002]. The possible obliquity forcing in the $\delta^{18}\text{O}$ record (see Figure 14) is in this case an indication of the waxing and waning of ice sheets and therefore global climate. The dominant obliquity signal in the $\delta^{18}\text{O}$ record is not unexpected for the late Burdigalian, since the East Antarctic ice sheet was already developed [e.g. Zachos *et al.*, 2008; Potter and Szatmari, 2009].

One should take into account that these bulk isotope records are strongly influenced by faunal compositions and that therefore some variations or changes can be controlled by change in fauna instead of a Mediterranean isotope change.

10.3 Onset Megabeds

The depositional system experienced some major change at the onset of the Megabeds, however, the cause of this change is yet to be found. Based on the insolation curve, high amplitude variations in precession (and therefore insolation) are causing prominent marl-limestones alternations and when the precession amplitude decreases, the Megabeds can be formed. This might be applicable for the Megabeds studied in this paper, but based on the preliminary tuning of the other Megabeds [F.J. Hilgen, S.K. Hüsing and E. Turco, pers. comm.] this is not applicable, since the eccentricity amplitude increases significantly.

Early to Middle Miocene sea level reconstructions show several rapid large-scale fluctuations [Haq *et al.*, 1987], of which only TB2.3 occurs during the same time interval as the Megabeds. However, TB2.3 is correlated to Mi2, which is present close to the base of the Langhian [Iaccarino *et al.*, 2011].

One of the criteria for the Langhian GSSP (Global Stratotype Section and Point) is the C5Cn/C5Br reversal, dated at *ca.* 15.974 Ma [Hilgen *et al.*, 2012], which is present at the top of Megabed IV. During the same time interval, the Mediterranean region is also strongly influenced by the reopening and closure of the eastern gateway. During the Early Miocene the *Gomphotherium* Landbridge is formed [Harzhauser *et al.*, 2007], but during the Middle Miocene Climatic Optimum the Mesopotamian Trough might still have connected the Indian Ocean with the proto-Mediterranean [Harzhauser *et al.*, 2007]. Unfortunately, the age of this Mesopotamian Trough is poorly constrained and therefore the causal relation with the formation of the Megabeds remains uncertain. It is however the most promising explanation of the sudden appearance of these prominent Megabeds.

10.4 Rock magnetism

The IRM interpretation of MCSS did not replicate the IRM results of the younger La Vedova and Monte dei Corvi sections [Hüsing *et al.*, 2009a, 2010; Mourik *et al.*, 2010], where a component with a low DP (thus a narrow grain size distribution) is found, characteristic for magnetotactic bacteria. Therefore it remains slightly uncertain whether the component with the lower DP (between 0.25 and 0.31 log₁₀ mT) is carrying a syn-depositional signal as has been demonstrated by e.g. Hüsing *et al.*, (2009a). The clear separation between normal and reverse polarity zones (in an almost antipodal matter) and a clear decrease towards the origin in most samples are indicative of a reliable polarity. Further rock magnetic analysis (such as Scanning Electron Microscopy) is required to confirm the reliability of the samples.

10.5 Global correlation silica

Enhanced biogenic opal preservation is not unusual for late Early Miocene sediments found in e.g. the Apennines [Montanari *et al.*, 1997a; Odin *et al.*, 1997], DSDP cores [Woodruff and Savin, 1989] or at the Californian coast [e.g. Isaacs, 1982]. This is likely caused by increased upwelling and therefore higher export productivity as is characteristic for the latest Early Miocene. At the same time the locations of dominant opal preservation changed, probably caused by a global reorganisation of ocean circulation [Kender *et al.*, 2008], resulting in a large-scale “silica switch” [Keller and Barron, 1983; Barron and Baldauf, 1990]. After this switch, the dominant silica production was located in the Indo-Pacific Ocean, instead of the North Atlantic [Barron and Baldauf, 1990].

The reorganisation of ocean circulation is not yet completely understood, but it is probably caused by an increase in northern hemisphere deep water formation [Pagani *et al.*, 2000; Cortese *et al.*, 2004]. The exact cause for the increase in deep water formation is yet unknown, it can be caused by the development of ice sheets [Cortese *et al.*, 2004], but also by the final closure of the Tethys ocean [Jones, 2006].

It should be noticed that increased activity of the African and Pacific Superplumes is also presented as a cause for the climate change during the Middle Miocene [Potter and Szatmari, 2009], but these large-scale global processes are poorly understood and consequently the causal relation is not proven. Also faster spreading rates, as presented by Potter and Szatmari, 2009, cannot be observed in tuned spreading rate records [Hüsing *et al.*, 2010].

11. Conclusions

The marl-limestone alternations (with corresponding proxy variations) of the MCSS composite section are astronomically forced and are consequently used for an astronomical tuning between *ca.* 17.08 and 16.18 Ma. This tuning uses the good match between the interference patterns in the Ca/Al and Rb/Sr ratios and those of the La2001_(1,0.9) solution. The ages of reversals C5Cn.3n (o) to C5Cn.1n (o) are improved and because of the robust tuning, these ages should replace the GTS2012 ages. Furthermore, the recognition of CM1 to CM3a in the $\delta^{13}\text{C}$ record is in agreement with previous findings that 405 kyr eccentricity cycles are imprinted in the Monterey Excursion. CM1 coincides with the base of the MMCO, which has also been recognized in the $\delta^{18}\text{O}$ record. Even though the global climate changes significantly during Miocene times, the precession dominated climate system, responsible for Mediterranean sapropel formation is already active during late Burdigalian times.

12. Acknowledgements

First of all, I thank Silja Hüsing for her supervision with this project, assistance in the field and major improvements in early drafts of the manuscript. Furthermore, Wout Krijgsman is thanked for the endless support and enthusiasm for this project. The many discussions with Frits Hilgen and Christian Zeeden and their assistance in the field are greatly appreciated. Jörn Wotzlaw is thanked for his assistance in the field, Arnold van Dijk for his support with the isotope measurements and Eric Kuikman for kindly providing data of the C5Dn (y) reversal.

13. References

- Abels, H. A., F. J. Hilgen, W. Krijgsman, R. W. Kruk, I. Raffi, E. Turco, and W. J. Zachariasse (2005), Long-period orbital control on middle Miocene global cooling: Integrated stratigraphy and astronomical tuning of the Blue Clay Formation on Malta, *Paleoceanography*, 20, 1–17, doi:10.1029/2004PA001129.
- Assorgia, A., L. S. Chan, A. Deino, C. Garbarino, A. Montanari, R. Rizzo, and S. Tocco (1994), Volcanogenic and paleomagnetic studies on the Cenozoic calc-alkalic eruptive sequence of Monte Ferru (Bosa, mid-western Sardinia), in *Miocene Stratigraphy of Italy and Adjacent Regions*, edited by R. Coccioni, A. Montanari, and G. S. Odin, pp. 17–29.
- Barron, J. A., and J. Baldauf (1990), Development of biosiliceous sedimentation in the North Pacific during the Miocene and Early Pliocene, in *Pacific Neogene events: their timing, nature and interrelationships*, edited by R. Tsuchi, pp. 43–63, University of Tokyo Press, Tokyo.
- Bartlett, M. S. (1950), Periodogram analysis and continuous spectra, *Biometrika*, 37, 1–16.
- Beccaluva, L., G. Bianchini, and F. Siena (2004), Tertiary-Quaternary volcanism and tectono-magmatic evolution in Italy, in *Geology of Italy, Special Volume of the Italian Geological Society for the IGC 32 Florence*, edited by U. Crescenti, S. D'Offizi, S. Merlini, and L. Sacchi, pp. 153–160, Rome.
- Billups, K., and D. P. Schrag (2002), Paleotemperatures and ice volume of the past 27 Myr revisited with paired Mg/Ca and $^{18}\text{O}/^{16}\text{O}$ measurements on benthic foraminifera, *Paleoceanography*, 17(1), 1–11.
- Billups, K., H. Pälike, J. E. T. Channell, J. C. Zachos, and N. J. Shackleton (2004), Astronomic calibration of the late Oligocene through early Miocene geomagnetic polarity time scale, *Earth and Planetary Science Letters*, 224(1-2), 33–44, doi:10.1016/j.epsl.2004.05.004.
- Blackman, R. B., and J. W. Tukey (1958), The Measurement of Power Spectra from the Point of View of Communications Engineering, *The Bell System Technical Journal*, 37(1-2), 185–569.

Blakely, R. J. (1974), Geomagnetic Reversals and Crustal Spreading Rates During the Miocene, *Journal of Geophysical Research*, 79(20), 2979–2985, doi:10.1029/JB079i020p02979.

Calvert, S. ., and T. . Pedersen (1993), Geochemistry of Recent oxic and anoxic marine sediments: Implications for the geological record, *Marine Geology*, 113, 67–88, doi:10.1016/0025-3227(93)90150-T.

Clement, B. M. (2004), Dependence of the duration of geomagnetic polarity reversals on site latitude, *Nature*, 428(6983), 637–40, doi:10.1038/nature02459.

Coccioni, R., and A. Montanari (1992), The “Livello Piero della Francesca” in the Umbria-Marche Apennines, Italy: a regional volcaniclastic marker bed at the boundary between the Bisciaro and the Schlier/Marne con Cerrognna formations (Lower Miocene), in *Volume of Abstracts and Field Trips, Interdisciplinary Geological Conference on the Miocene Epoch with emphasis on the Umbria-Marche sequence (I.U.G.S., Subcommission on Geochronology, Miocene Columbus Project)*, edited by A. Montanari, R. Coccioni, and G. S. Odin, pp. 41–42, Ancona.

Cooke, P. J., C. S. Nelson, and M. P. Crundwell (2008), Miocene isotope zones, paleotemperatures, and carbon maxima events at intermediate water-depth, Site 593 , Southwest Pacific, *New Zealand Journal of Geology & Geophysics*, 51(1), 1–22, doi:10.1080/00288300809509846.

Cortese, G., R. Gersonde, C.-D. Hillenbrand, and G. Kuhn (2004), Opal sedimentation shifts in the World Ocean over the last 15 Myr, *Earth and Planetary Science Letters*, 224(3-4), 509–527, doi:10.1016/j.epsl.2004.05.035.

Diester-Haass, L., K. Billups, D. R. Gröcke, L. François, V. Lefebvre, and K. C. Emeis (2009), Mid-Miocene paleoproductivity in the Atlantic Ocean and implications for the global carbon cycle, *Paleoceanography*, 24(1), 1–19, doi:10.1029/2008PA001605.

Ellwood, B. B., R. E. Crick, A. El Hassani, S. L. Benoist, and R. H. Young (2000), Magnetosusceptibility event and cyclostratigraphy method applied to marine rocks : Detrital input versus carbonate productivity, *Geology*, 28(12), 1135–1138, doi:10.1130/0091-7613(2000)28<1135.

Farge, M. (1992), Wavelet transforms and their applications to turbulence, *Annual Reviews of Fluid Mechanics*, 24, 395–457.

Foucault, A., and F. Mélières (2000), Palaeoclimatic cyclicity in central Mediterranean Pliocene sediments: the mineralogical signal, *Palaeogeography, Palaeoclimatology, Palaeoecology*, 158(3-4), 311–323, doi:10.1016/S0031-0182(00)00056-0.

Guerrera, F., M. Tramontana, U. Donatelli, and F. Serrano (2012), Space/time tectono-sedimentary evolution of the Umbria-Romagna-Marche Miocene Basin (Northern Apennines, Italy): a foredeep model, *Swiss Journal of Geosciences*, 105(3), 325–341, doi:10.1007/s00015-012-0118-0.

Haq, B. U., J. Hardenbol, and P. R. Vail (1987), Chronology of Fluctuating Sea Levels Since the Triassic, *Science*, 235(4793), 1156–1167.

Harzhauser, M., A. Kroh, O. Mandic, W. E. Piller, U. Göhlich, M. Reuter, and B. Berning (2007), Biogeographic responses to geodynamics: A key study all around the Oligo–Miocene Tethyan Seaway, *Zoologischer Anzeiger - A Journal of Comparative Zoology*, 246, 241–256, doi:10.1016/j.jcz.2007.05.001.

Hastings, D. W., S. R. Emerson, and A. C. Mix (1996), Vanadium in foraminiferal calcite as a tracer for changes in the areal extent of reducing sediments, *Paleoceanography*, 11(6), 665–678.

Heier, K. S., and G. K. Billings (1970), Rubidium, in *Handbook of Geochemistry*, edited by K. H. Wedepohle, pp. 37B1–37K3, Springer, Berlin/Heidelberg.

Heirtzler, J. R., G. O. Dickson, E. M. Herron, W. C. I. Pitman, and X. Le Pichon (1968), Marine Magnetic Anomalies, Geomagnetic Field Reversals, and Motions of the Ocean Floor and Continents, *Journal of Geophysical Research*, 73(6), 2119–2136.

Heslop, D., G. McIntosh, and M. J. Dekkers (2004), Using time- and temperature-dependent Preisach models to investigate the limitations of modelling isothermal remanent magnetization acquisition curves with cumulative log Gaussian functions, *Geophysical Journal International*, 157(1), 55–63, doi:10.1111/j.1365-246X.2004.02155.x.

Hilgen, F. J. (1991), Extension of the astronomically calibrated (polarity) time scale to the Miocene/Pliocene boundary, *Earth and Planetary Science Letters*, 107(2), 349–368, doi:10.1016/0012-821X(91)90082-S.

Hilgen, F. J., L. J. Lourens, and J. A. Van Dam (2012), The Neogene Period, in *The Geological Time Scale*, edited by F. M. Gradstein, J. G. Ogg, M. D. Schmitz, and G. M. Ogg, pp. 923–978, Elsevier B.V.

Holbourn, A., W. Kuhnt, M. Schulz, J.-A. Flores, and N. Andersen (2007), Orbitally-paced climate evolution during the middle Miocene “Monterey” carbon-isotope excursion, *Earth and Planetary Science Letters*, 261(3-4), 534–550, doi:10.1016/j.epsl.2007.07.026.

Hüsing, S. K., F. J. Hilgen, H. A. Aziz, and W. Krijgsman (2007), Completing the Neogene geological time scale between 8.5 and 12.5 Ma, *Earth and Planetary Science Letters*, 253, 340–358, doi:10.1016/j.epsl.2006.10.036.

Hüsing, S. K., M. J. Dekkers, C. Franke, and W. Krijgsman (2009a), The Tortonian reference section at Monte dei Corvi (Italy): evidence for early remanence acquisition in greigite-bearing sediments, *Geophysical Journal International*, 179(1), 125–143, doi:10.1111/j.1365-246X.2009.04301.x.

Hüsing, S. K., K. F. Kuiper, W. Link, F. J. Hilgen, and W. Krijgsman (2009b), The upper Tortonian–lower Messinian at Monte dei Corvi (Northern Apennines, Italy): Completing a Mediterranean reference section for the Tortonian Stage, *Earth and Planetary Science Letters*, 282(1-4), 140–157, doi:10.1016/j.epsl.2009.03.010.

Hüsing, S. K., A. Casella, F. J. Hilgen, W. Krijgsman, K. F. Kuiper, E. Turco, and D. Wilson (2010), Astrochronology of the Mediterranean Langhian between 15.29 and 14.17 Ma, *Earth and Planetary Science Letters*, 290(3-4), 254–269, doi:10.1016/j.epsl.2009.12.002.

Iaccarino, S. M. et al. (2011), High-resolution integrated stratigraphy of the upper Burdigalian-lower Langhian in the Mediterranean : the Langhian historical stratotype and new candidate sections for defining its GSSP, *Stratigraphy*, 8, 199–215.

Isaacs, C. M. (1982), Influence of rock composition on kinetics of silica phase changes in the Monterey Formation, Santa Barbara area, California, *Geology*, 10, 304–308, doi:10.1130/0091-7613(1982)10<304.

Jarboe, N. A., R. S. Coe, P. R. Renne, and J. M. G. Glen (2010), The age of the Steens reversal and the Columbia River Basalt Group, *Chemical Geology*, 274(3-4), 158–168, doi:10.1016/j.chemgeo.2010.04.001.

Jones, R. W. (2006), *Applied palaeontology*, Cambridge University Press, Cambridge.

Keller, G., and J. A. Barron (1983), Paleoceanographic implications of Miocene deep-sea hiatuses, *Geological Society of America Bulletin*, 94, 590–613, doi:10.1130/0016-7606(1983)94<590.

Kender, S., M. A. Kaminski, and R. W. Jones (2008), Early to middle Miocene foraminifera from the deep-sea Congo Fan, offshore Angola, *Micropaleontology*, 54(6), 477–568.

Kirschvink, J. L. (1980), The least-squares line and plane and the analysis of palaeomagnetic data, *Geophysical Journal of the Royal Astronomical Society*, 62(3), 699–718.

Kocsis, L., T. W. Vennemann, D. Fontignie, C. Baumgartner, A. Montanari, and B. Jelen (2008), Oceanographic and climatic evolution of the Miocene Mediterranean deduced from Nd, Sr, C, and O isotope compositions of marine fossils and sediments, *Paleoceanography*, 23(4), PA4211, doi:10.1029/2007PA001540.

Krom, M. D., A. Michard, R. A. Cliff, and K. Strohle (1999), Sources of sediment to the Ionian Sea and western Levantine basin of the Eastern Mediterranean during S-1 sapropel times, *Marine Geology*, 160(1-2), 45–61, doi:10.1016/S0025-3227(99)00015-8.

Krs, M., F. Novak, M. Krsova, P. Pruner, L. Kouklikova, and J. Jansa (1992), Magnetic properties and metastability of greigite-smythite mineralization in brown-coal basins of the Krusne hory Piedmont, Bohemia, *Physics of the Earth and Planetary Interiors*, 70, 273–287.

Kruiver, P. P., M. J. Dekkers, and D. Heslop (2001), Quantification of magnetic coercivity components by the analysis of acquisition curves of isothermal remanent magnetisation, *Earth and Planetary Science Letters*, 189, 269–276.

Kryc, K. A., R. W. Murray, and D. W. Murray (2003), Al-to-oxide and Ti-to-organic linkages in biogenic sediment: relationships to paleo-export production and bulk Al/Ti, *Earth and Planetary Science Letters*, 211, 125–141, doi:10.1016/S0012-821X(03)00136-5.

Laskar, J. (2001), Astronomical Solutions for Paleoclimate Studies, in *AGU Fall Meeting*, p. Abstracts U11A–01.

Laskar, J., P. Robutel, F. Joutel, M. Gastineau, A. C. M. Correia, and B. Levrard (2004), Astrophysics A long-term numerical solution for the insolation, *Astronomy & Astrophysics*, 285, 261–285, doi:10.1051/0004-6361.

Laskar, J., A. Fienga, M. Gastineau, and H. Manche (2011), La2010: a new orbital solution for the long-term motion of the Earth, *Astronomy & Astrophysics*, 532, A89, doi:10.1051/0004-6361/201116836.

Lourens, L. J., R. Wehausen, and H. J. Brumsack (2001), Geological constraints on tidal dissipation and dynamical ellipticity of the Earth over the past three million years., *Nature*, 409, 1029–1033, doi:10.1038/35059062.

Lourens, L. J., F. J. Hilgen, N. J. Shackleton, J. Laskar, and D. Wilson (2004), The Neogene Period, in *A Geological Time Scale*, edited by F. M. Gradstein, J. G. Ogg, and A. G. Smith, pp. 409–440, Cambridge University Press.

Mader, D., A. Montanari, C. Koeberl, R. Handler, and R. Coccioni (2001), $^{40}\text{Ar}/^{39}\text{Ar}$ dating of a Langhian biotite-rich clay layer in the Conero Riviera, Ancona, Italy, *Earth and Planetary Science Letters*, 194, 111–126.

Miller, K. G., and G. S. Mountain (1996), Drilling and Dating New Jersey Oligocene-Miocene Sequences: Ice Volume, Global Sea Level, and Exxon Records, *Science*, 271, 1092–1095.

Miller, K. G., J. D. Wright, and G. Fairbanks (1991), Unlocking the Ice House: Oligocene-Miocene oxygen isotopes, eustasy, and margin erosion, *Journal of Geophysical Research*, 96, 6829–6848.

Montanari, A., D. M. Bice, R. Capo, R. Coccioni, A. Deino, D. J. DePaolo, L. Emmanuel, S. Monechi, M. Renard, and D. Zevenboom (1997a), C3. Integrated stratigraphy of the Chattian to Mid-Burdigalian pelagic sequence of the Contessa valley (Gubbio, Italy), in *Miocene Stratigraphy: An Integrated Approach (Developments in Palaeontology and Stratigraphy)*, edited by A. Montanari, G. S. Odin, and R. Coccioni, pp. 249–277, Elsevier B.V.

Montanari, A. et al. (1997b), Integrated stratigraphy of the Middle and Upper Miocene pelagic sequence of the Conero Riviera (Marche region, Italy), in *Miocene Stratigraphy: An Integrated Approach (Developments in*

Palaeontology and Stratigraphy), edited by A. Montanari, G. S. Odin, and R. Coccioni, pp. 409–450, Elsevier B.V.

Morford, J. L., and S. Emerson (1999), The geochemistry of redox sensitive trace metals in sediments, *Geochimica et Cosmochimica Acta*, 63(11/12), 1735–1750.

Mourik, A. A., J. F. Bijkerk, A. Cascella, S. K. Hüsing, F. J. Hilgen, L. J. Lourens, and E. Turco (2010), Astronomical tuning of the La Vedova High Cliff section (Ancona, Italy)—Implications of the Middle Miocene Climate Transition for Mediterranean sapropel formation, *Earth and Planetary Science Letters*, 297(1-2), 249–261, doi:10.1016/j.epsl.2010.06.026.

Mullender, T. A. T., A. J. van Velzen, and M. J. Dekkers (1993), Continuous drift correction and separate identification of ferromagnetic and paramagnetic contributions in thermomagnetic runs, *Geophysical Journal International*, 114, 663–672.

Odin, G. S., A. Amorosi, F. Tateo, R. Coccioni, M. Cosca, A. Negri, G. A. Pini, and J. C. Hunziker (1997), C2. Integrated stratigraphy (biostratigraphy and geochronology) of the Early Miocene sequence from the Emilian Apennines (Italy), in *Miocene Stratigraphy: An Integrated Approach (Developments in Palaeontology and Stratigraphy)*, edited by A. Montanari, G. S. Odin, and R. Coccioni, pp. 221–247, Elsevier B.V.

Pagani, M., M. A. Arthur, and H. Freeman (2000), Variations in Miocene phytoplankton growth rates in the southwest Atlantic: Evidence for changes in ocean circulation, *Paleoceanography*, 15(5), 486–496.

Paillard, D., L. Labeyrie, and P. Yiou (1996), Macintosh Program performs time-series analysis, *Eos, Transactions American Geophysical Union*, 77(39), 379, doi:10.1029/96EO00259. [online] Available from: <http://doi.wiley.com/10.1029/96EO00259>

Pälike, H., and N. J. Shackleton (2000), Constraints on astronomical parameters from the geological record for the last 25 Myr, *Earth and Planetary Science Letters*, 182, 1–14.

Passier, H. F., G. J. de Lange, and M. J. Dekkers (2001), Magnetic properties and geochemistry of the active oxidation front and the youngest sapropel in the eastern Mediterranean Sea, *Geophysical Journal International*, 145, 604–614, doi:10.1046/j.0956-540x.2001.01394.x.

Potter, P. E., and P. Szatmari (2009), Global Miocene tectonics and the modern world, *Earth-Science Reviews*, 96(4), 279–295, doi:10.1016/j.earscirev.2009.07.003.

Roberts, A. P. (1995), Magnetic properties of sedimentary greigite (Fe₃S₄), *Earth and Planetary Science Letters*, 134, 227–236.

Robertson, D. J., and D. E. France (1994), Discrimination of remanence-carrying minerals in mixtures, using isothermal remanent magnetisation acquisition curves, *Physics of the Earth and Planetary Interiors*, 82(3-4), 223–234, doi:10.1016/0031-9201(94)90074-4.

Rögl, F. (1998), Palaeogeographic Considerations for Mediterranean and Paratethys Seaways (Oligocene to Miocene), *Annalen des Naturhistorischen Museums in Wien*, 99A, 279–310.

Van Santvoort, P. J. M., G. J. de Lange, J. Thomson, H. Cussen, T. R. S. Wilson, M. D. Krom, and K. Ströhle (1996), Active post-depositional oxidation of the most recent sapropel (S1) in sediments of the eastern Mediterranean Sea, *Geochimica et Cosmochimica Acta*, 60(21), 4007–4024.

Scott, G. H., C. S. Nelson, and H. H. Stone (1995), Planktic foraminiferal events in early Miocene Zones N.6 and N.7 at southwest Pacific DSDP Site 593: relation with climatic changes in oxygen isotope Zone Mi1b, *Marine Micropaleontology*, 25, 29–45.

Torrence, C., and G. P. Compo (1998), A Practical Guide to Wavelet Analysis, *Bulletin of the American Meteorological Society*, 79(1), 61–78.

Turco, E., A. Cascella, R. Gennari, F. J. Hilgen, S. M. Iaccarino, and L. Sagnotti (2011), Integrated stratigraphy of the La Vedova section (Conero Riviera, Italy) and implications for the Burdigalian/Langhian boundary, *Stratigraphy*, 8, 89–110.

Vasiliev, I., M. J. Dekkers, W. Krijgsman, C. Franke, C. G. Langereis, and T. A. T. Mullender (2007), Early diagenetic greigite as a recorder of the palaeomagnetic signal in Miocene-Pliocene sedimentary rocks of the Carpathian foredeep (Romania), *Geophysical Journal International*, 171(2), 613–629, doi:10.1111/j.1365-246X.2007.03560.x.

Vasiliev, I., C. Franke, J. D. Meeldijk, M. J. Dekkers, C. G. Langereis, and W. Krijgsman (2008), Putative greigite magnetofossils from the Pliocene epoch, *Nature Geoscience*, 1(11), 782–786, doi:10.1038/ngeo335.

Weber, S. L., and E. Tuenter (2011), The impact of varying ice sheets and greenhouse gases on the intensity and timing of boreal summer monsoons, *Quaternary Science Reviews*, 30(3-4), 469–479, doi:10.1016/j.quascirev.2010.12.009.

Wehausen, R., and H.-J. Brumsack (2000), Chemical cycles in Pliocene sapropel-bearing and sapropel-barren eastern Mediterranean sediments, *Palaeogeography, Palaeoclimatology, Palaeoecology*, 158, 325–352, doi:10.1016/S0031-0182(00)00057-2.

Weldeab, S., W. Siebel, R. Wehausen, K.-C. Emeis, G. Schmiedl, and C. Hemleben (2003), Late Pleistocene sedimentation in the Western Mediterranean Sea: implications for productivity changes and climatic conditions in the catchment areas, *Palaeogeography, Palaeoclimatology, Palaeoecology*, 190, 121–137, doi:10.1016/S0031-0182(02)00602-8.

Woodruff, F., and S. M. Savin (1989), Miocene Deepwater Oceanography, *Paleoceanography*, 4(1), 87–140.

Woodruff, F., and S. M. Savin (1991), Mid-Miocene isotope stratigraphy in the deep sea: high-resolution correlations, paleoclimatic cycles, and sediment preservation, *Paleoceanography*, 6(6), 755–806.

Zachos, J. C., M. Pagani, L. Sloan, E. Thomas, and K. Billups (2001), Trends, rhythms, and aberrations in global climate 65 Ma to present., *Science*, 292, 686–693, doi:10.1126/science.1059412.

Zachos, J. C., G. R. Dickens, and R. E. Zeebe (2008), An early Cenozoic perspective on greenhouse warming and carbon-cycle dynamics., *Nature*, 451(7176), 279–283.

Zijderveld, J. D. A. (1967), A.C. demagnetization of rocks: analysis of results, in *Developments in Solid Earth Geosciences Methods in Paleomagnetism*, edited by S. K. Runcon, Elsevier Publishing Company, Amsterdam.

Appendix 1

Table 4: The maxima in Ca/Al at a certain position are correlated to insolation maxima of a certain age.

Position (m)	Age (ka)
75.76	16188
73.89	16207
72.11	16225
71.17	16245
70.18	16266
68.38	16297
66.8	16315
65.42	16338
64.36	16359
63.12	16382
61.37	16406
59.61	16429
58.72	16452
57.81	16472
56.7	16498
54.42	16522
52.58	16545
50.96	16566
49.88	16583
48.94	16598
46.72	16621
45.45	16642
43.34	16666
41.86	16692
40.52	16713
39.41	16736
37.52	16758
36.57	16783
34.74	16806
33.66	16827
32.13	16850
29.64	16873
27.1	16898
24.72	16919
22.72	16941
20.44	16961
15.87	16990
12.34	17017
9.11	17032
5.44	17052
2.94	17069